Experimental Validation of Numerical Simulations for An Acoustic Liner in Grazing Flow

Christopher K. W. Tam[1], Nikolai N. Pastouchenko[2]
Florida State University, Tallahassee, FL 32306-4510, USA

Michael G. Jones[3], Willie R. Watson[4]
NASA Langley Research Center, Hampton, VA 23681-2199, USA

A coordinated experimental and numerical simulation effort is carried out to improve our understanding of the physics of acoustic liners in a grazing flow as well our computational aeroacoustics (CAA) method prediction capability. A numerical simulation code based on advanced CAA methods is developed. In a parallel effort, experiments are performed using the Grazing Flow Impedance Tube at the NASA Langley Research Center. In the experiment, a liner is installed in the upper wall of a rectangular flow duct with a 2 inch by 2.5 inch cross section. Spatial distribution of sound pressure levels and relative phases are measured on the wall opposite the liner in the presence of a Mach 0.3 grazing flow. The computer code is validated by comparing computed results with experimental measurements. Good agreements are found. The numerical simulation code is then used to investigate the physical properties of the acoustic liner. It is shown that an acoustic liner can produce self-noise in the presence of a grazing flow and that a feedback acoustic resonance mechanism is responsible for the generation of this liner self-noise. In addition, the same mechanism also creates additional liner drag. An estimate, based on numerical simulation data, indicates that for a resonant liner with a 10% open area ratio, the drag increase would be about 4% of the turbulent boundary layer drag over a flat wall.

1. Introduction

The advent of fast and powerful computers has made it possible to investigate the characteristics of acoustic liners computationally. This approach offers a useful complement to traditional experimental investigation. Experimental studies are indispensable for exploratory work on liner properties. They are also necessary for the validation of computer simulation codes.

This paper provides the results of a combined experimental and numerical investigation of the properties of acoustics liners in a grazing flow. The experiments were carried out using the Grazing Flow Impedance Tube (GFIT) at the NASA Langley Research Center. The GFIT has a rectangular cross-section and the test liner is installed into the upper wall. The measured mean flow velocity profile at the inflow boundary provides the basic information needed for mean flow computation in the presence of the test liner. A microphone array is flush-mounted in the wall opposite the liner and the measured acoustic pressure distribution is used to evaluate the damping characteristics of the liner. This same set of data is also used for computer code validation. Upon satisfactory validation of the computer code, the complete space-time data from the numerical simulations are used to investigate liner properties in detail.

There have been a number of fundamental experimental investigations and numerical simulations of the properties of acoustic liners in the past. Here an investigation is referred to as in the fundamental category if it uses a first principle approach and accounts for the internal structure of a liner. These studies do not represent a liner

---

[1] Robert O. Lawton Distinguished Professor, Department of Mathematics, Fellow AIAA.
[2] Research Associate, Department of Mathematics, Currently GE Global Research Center, Senior Member AIAA.
[3] Senior Research Scientist, Structural Acoustics Branch, Research Directorate. Associate Fellow AIAA.
[4] Senior Research Scientist, Computational Aerosciences Branch, Research Directorate. Associate Fellow AIAA.

merely as an impedance surface. Early experimental work concentrated on the understanding of the interaction of sound and the face sheet of a liner. To simplify the problem, an orifice was used in lieu of a face sheet. Some of these experiments were carried out by Sivian[1], Ingard and Labate[2], and Ingard and Ising[3]. In a comprehensive paper, Melling[4] summarized the findings of all the early experimental and theoretical work. More recent experimental studies by Goldman and Ponton[5], Kompenhans and Ronneberger[6], Kooi and Sarin[7], Walker and Charwat[8], Worraker and Halliwell[9] and Malmary and Carbonne[10] included the effects of grazing flow.

An acoustic liner has a complex internal structure. Because of the geometrical complexities involved, analytical methods, invariably, encounter difficulties in solving the Navier-Stokes equations for the flow and acoustic fields around the liner. This makes numerical simulation more tractable for computing the acoustic properties of a liner. Tam and Kurbatskii[11] were one of the first to carry out a direct numerical simulation of a train of acoustic waves impinging on a wall-mounted resonator. A number of simplifications were adopted in this early work. The simplifications included the use of a single two-dimensional slit resonator model without a grazing flow. It was found that sound absorption by the resonator could be divided into two regimes. At low sound-pressure-level (SPL), acoustic dissipation is caused mainly by the excited oscillatory boundary layer around the opening of the resonator. Generally speaking, in this regime, the sound absorption rate is low. At higher SPL, vortex shedding takes places at the corners of the opening of the resonator. This is accompanied by an enhanced acoustic dissipation. The mechanism of dissipation is attributed to the conversion of incident acoustic wave energy into the rotational kinetic energy of the shed vortices. The shed vortices are subsequently dissipated by the molecular viscosity of the gas. This finding was confirmed experimentally in a later investigation by Tam, Kurbatskii, Ahuja and Gaeta[12]. A similar simulation was subsequently repeated by Zhang and Bodany[13]. To provide further support to this finding, a comprehensive experimental and computational study of the interaction of sound waves and a resonator in a normal incidence impedance tube was performed by Tam, Ju, Jones, Watson and Parrott[14]. Both normal and beveled slits of different slit widths at a number of discrete incident sound frequencies as well as broadband incident sound waves were used. The results confirmed that, indeed, there were two regimes of sound absorption. In addition, it was found that there were good agreements between experimentally measured resonator impedance and those computed by numerical simulation. The good agreements provided confidence in the use of numerical simulation in liner technology research.

Since the above mentioned work, numerical simulations of sound interaction with a resonator in three dimensions have been performed by a number of investigators including Tam, Ju, Jones, Watson and Parrott[15] and Zhang and Bodony [16]. More recent work including a grazing flow were presented by Roche, Leyekian, Delattre, and Vuillot[17], Tam, Ju and Walker[18] and Roche, Vuillot, Leyekian, Delattre, Piot and Simon[19]. Zhang and Bodony[20] went a step further to add a time-evolving turbulent boundary layer in their simulation. Large eddy simulation (LES) methods were used to create the time evolving turbulent boundary layer. Thus, significant progress has been made in the effort to determine acoustic liner properties computationally. However, all the numerical simulations performed so far are confined to a single resonator.

One of the objectives of the present investigation is to conduct numerical simulation of an acoustic liner with multiple resonators. Because the simulation includes many resonators, their possible flow and acoustic interaction are taken into account. Also, when an incident acoustic wave passes over the liner, the wave is damped by each resonator. The accumulated damping effect is exhibited in the present experimental measurements and numerical simulation.

The purpose of installing acoustic liners in a jet engine is to damp out fan noise. However, in this investigation, it is found that a liner in a grazing flow can create noise on its own. We will refer to this noise as liner self-noise. Fortunately, the frequency of liner self-noise is very high and hence is of no importance as far as engine noise certification is concerned. The mechanism by which liner self-noise is generated is found to be related to a feedback loop. Details of the self-noise generation mechanism are reported in this paper, and it is shown that the same mechanism is also responsible for creating additional drag on the liner. For a liner with a typical face sheet open area of 10%, it is estimated that an increase of about 4% drag (based on turbulent boundary layer drag on a hard wall surface) could be realized.

The rest of this paper is as follows. Section 2 provides a description of the NASA GFIT and the liner used in the experiment and numerical simulation. Section 3 describes the computational model and computational algorithm employed in the present study. In Section 4, numerical results and their comparisons with experimental

measurements are reported. Liner self-noise and additional liner drag are discussed in Section 5. The important effects of grazing flow on acoustic liner and resonator properties are also discussed in Section 5. Section 6 provides the primary conclusions resulting from this investigation.

2. Experimental Methods

An eight-chamber acoustic liner (see Fig. 1) was tested in the GFIT (see Fig. 2) for comparison with predictions conducted with the computational model that will be presented in section 3. The 16”-long frame is designed such that the partition spacing can be chosen to create numerous configurations. For the current investigation, the liner consists of eight identical segments. Each segment has 1.95”-long x 2.0”-wide x 2.2”-deep chambers, with a rigid wall back plate and a 0.062”-thick facesheet consisting of a single square-edged slit (total of 8 slits). The slits are 0.05” long and 2.0” wide, such that they span the full width of the liner. Finally, the segments are separated by 0.05”-thick partitions.

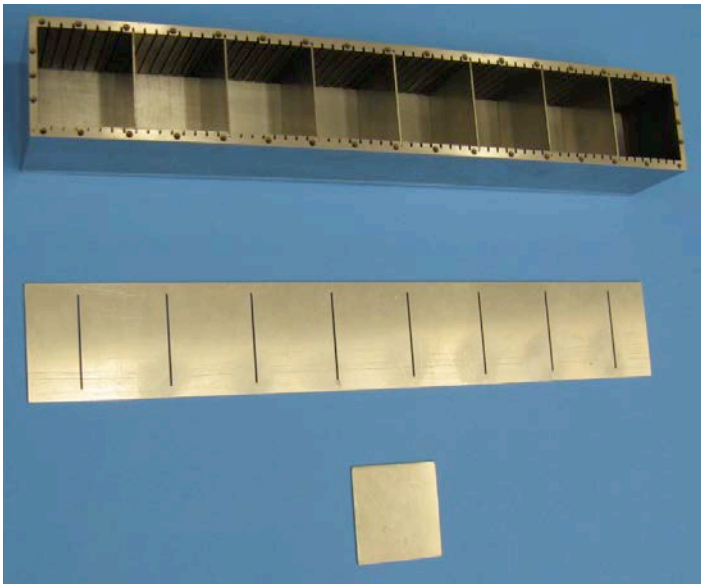

(a) Liner components (eight-segment frame, slit facesheet, partition).

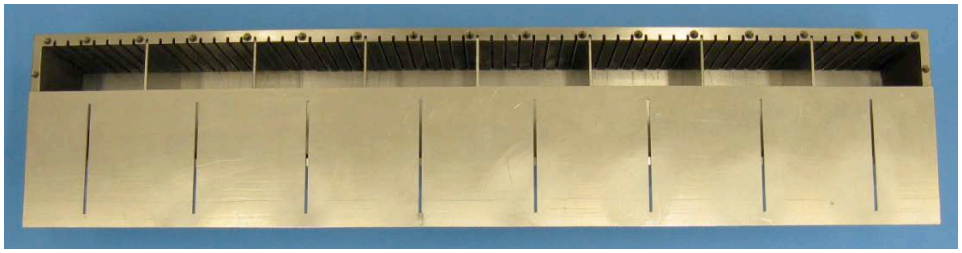

(b) Facesheet partially mounted onto frame.

Figure 1. Photographs of test liner.

The GFIT has a cross-sectional geometry of 2.0 in. x 2.5 in., and allows convenient evaluation of acoustic liners with lengths from 2.0 in. to 24.0 in. As depicted in Fig. 2, flow propagates from left to right. High pressure air is supplied on the upstream end, and a vacuum blower is located on the downstream end, such that the test window containing the acoustic liner is exposed to near-ambient pressure conditions for mean flows up to Mach 0.6. The surface of the test liner forms a portion (16.0 inches for the current investigation) of the upper wall of the flow duct. Eighteen acoustic drivers are mounted upstream of the test window, and are used to generate tones (one frequency at a time) at up to 150 dB over a frequency range of 0.4 to 3.0 kHz. Fifty-three microphones flush-mounted in the lower wall (opposite the liner) are used to measure the acoustic pressure field from 8.0 inches upstream of the liner leading edge to 16.0 inches downstream of the liner trailing edge (total length of 40.0 inches). For each data acquisition, 2000 averages on each microphone channel (blocks of 2048 data points per average) are

taken. To reduce the influence of flow noise, a cross-spectrum signal extraction method[21] is used to determine the amplitudes and phases at each of the microphone locations relative to the amplitude and phase at the reference microphone location. For the current study, each liner configuration is tested using a tonal source (one frequency at a time) in the GFIT at centerline Mach numbers of 0.0 and 0.3, with source sound pressure levels of at least 140 dB, and at frequencies of 0.5 to 3.0 kHz in 0.5 kHz increments.

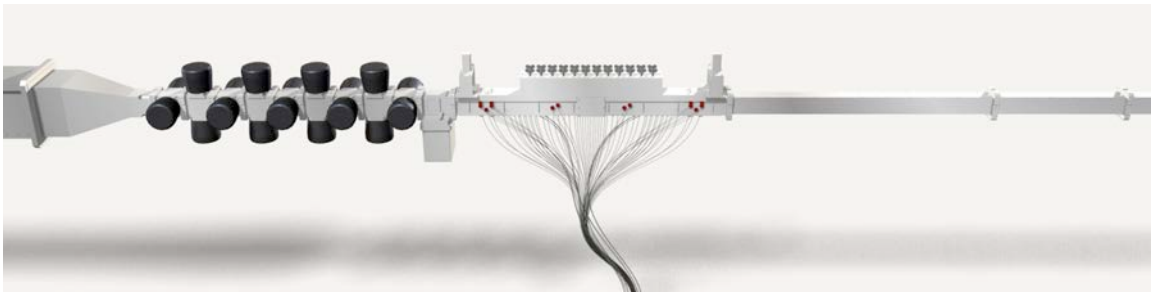

Figure 2. NASA Langley Grazing Flow Impedance Tube.

Comparisons of numerical and experimental results are provided in section 4. These comparisons include predicted and measured acoustic pressures (sound pressure level and phase) along the length of the liner. It should be noted that the computational method assumes the downstream termination to be anechoic. However, the GFIT termination is not fully anechoic, with an impedance spectrum that varies with test condition (mean flow Mach number, source frequency). Thus, to enable proper comparisons, the effects of reflections from the GFIT termination must be taken into account.

For each test condition, the acoustic impedance of the test liner is educed via the NASA impedance eduction process. This process has been previously presented in detail[22] and is based on the acoustic pressures measured with 53 microphones flush-mounted in the wall opposite the test liner. The model implemented within this impedance eduction process is based on assumptions that (1) the mean flow is uniform, (2) the surface impedance of the test liner is uniform, (3) the liner is local reacting, and (4) only planar acoustic waves exist at the source and duct termination planes.

3. Computation Model, Mesh Design and Computational Algorithm

One of the objectives of this work is to perform numerical simulations to determine the performance of an acoustic liner in the presence of grazing flow and grazing incident sound waves. Emphasis is on investigating the interaction of the mean flow and incident sound with an individual resonator of the liner, as well as the collective response of the resonators to incident acoustic waves. Once the computational code is validated, further numerical simulations are carried out to find possible new phenomena in such a combined flow and acoustic field.

An acoustic liner, generally, has a complex structure with numerous holes on the face sheet. Because of the structural complexity, an enormous amount of computing resources would be required to perform numerical simulations accurately. This is beyond the scope of the present investigation. To keep the computational requirements reasonable but still retaining the basic liner physics, a row of 8 slit resonators is chosen to form a liner in this study. Each slit has the dimension of 2 inches by 0.05 inches so that the aspect ratio of the slit is 40. This is a very large aspect ratio. It is, therefore, possible, as a first approximation, to regard the slit as two dimensional. For the GFIT, at sound frequencies below 3 kHz, the only propagating wave is the plane wave mode. It is to be noted that plane waves would automatically satisfy the GFIT side wall boundary condition. Since plane waves are essentially two dimensional, it follows that the overall problem under study may be regarded approximately as two dimensional. For its simplicity, a two dimensional computational model is adopted in the rest of this paper.

Fig. 3 shows the entire computational domain of the present numerical simulation. It consists of a grazing flow tube bounded at the two ends by non-reflecting boundary conditions implemented via Perfectly Matched Layers (PML). On the bottom wall of the rectangular tube is an acoustic liner. The liner is comprised of 8 slit resonators. Each resonator is connected to the grazing flow tube by a small slit of 0.05 inches width. The geometry of the liner is identical to that used in the experiment.

It should be noted that the computational model assumes the liner to be located on the lower wall. However, as indicated in Fig. 2, the experiment was conducted with the liner on the upper wall. Hence, the numerical results predicted for the upper wall, the wall opposite the liner, should be compared with the data measured on the lower wall of GFIT.

The design and selection of the present computational mesh and algorithm are guided by two criteria. The first is accuracy. That is, the computational code must have adequate spatial and temporal resolution to ensure that the numerical simulation contains all the essential physics of a grazing flow over an acoustic liner in the presence of incident sound. The second is that the choice of mesh sizes and the number of mesh points of the code is such that the code should run as fast as possible (in addition to being stable and accurate). That is, an effort is made to keep the total number of mesh points small but sufficient.

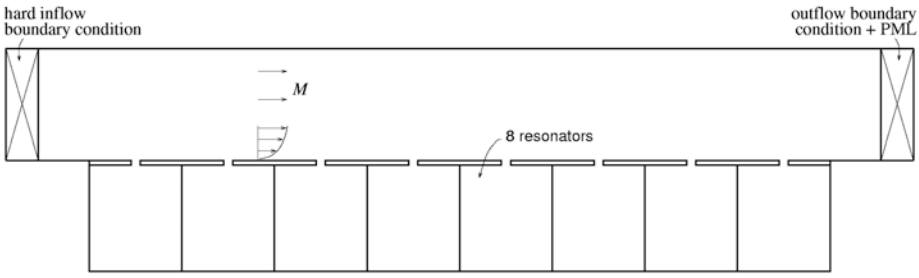

Figure 3. Computational domain including inflow and outflow boundary conditions for mean flow computation.

3.1 Mesh Design

In the present problem, vortex shedding at the openings of the liner resonators is an important damping mechanism for the incident acoustic waves. The presence of a turbulent boundary layer right over the acoustic liner is expected to have an influence on the interaction of sound and resonators. Thus the smallest mesh size is determined, in the present design, by the resolution needed to resolve the thickness of the Stokes layer at the openings of the resonators and the log layer of the turbulent boundary layer adjacent to the liner. To keep the total number of mesh points in the computational domain to a reasonable value, the highest computational frequency that the code can resolve is set at 3 kHz. That is, the thickness of the Stokes layer used in the mesh design is based on 3 kHz.

The fluid flow and acoustic field around an acoustic liner form a multi-scales problem. Around the openings of a resonant liner, viscous effects dominate. To resolve the oscillatory Stokes layer a mesh with a resolution of 7 mesh points per wavelength (using the 7-point Dispersion-Relation-Preserving (DRP) scheme[23]) is needed. Away from the walls, compressibility effects dominate. The length scale is the acoustic wavelength. As a result, the use of a relatively coarse mesh will offer sufficient resolution. Because of the multi-scale nature of the problem, the multi-size-mesh multi-time-step DRP scheme of Tam and Kurbatskii[24] (see also Tam[25]) is used. The computational mesh is, therefore, designed to support such a computation scheme.

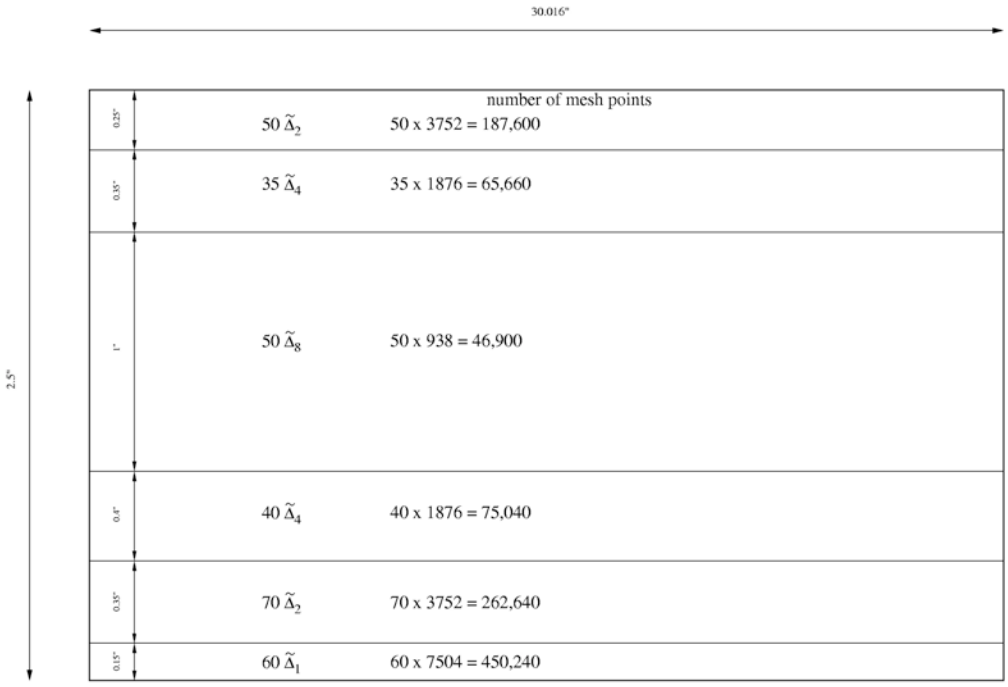

Figure 4. Basic mesh design in the grazing flow tube. The mesh sizes are as follows,
$\tilde{\Delta}_1 = 0.004\ in.$ x $0.0025\ in.$, $\tilde{\Delta}_2 = 0.008\ in.$ x $0.005\ in.$, $\tilde{\Delta}_4 = 0.016\ in.$ x 0.01 in.,
$\tilde{\Delta}_8 = 0.032\ in.$ x $0.02\ in.$

Fig. 4 shows the basic grid design inside the grazing flow tube without the resonators. The finest meshes are in the bottom layer where there is a turbulent boundary layer. The top mesh layer, adjacent to the top wall, has a spatial resolution equal to half of that of the very bottom layer. This choice is to save mesh points. It is justified because a good resolution of the turbulent boundary layer adjacent to the top wall is believed not critical to the overall problem. The total number of mesh points in the flow tube is 1.088 million. The basic mesh distribution will be modified when the resonators are added to the computational domain.

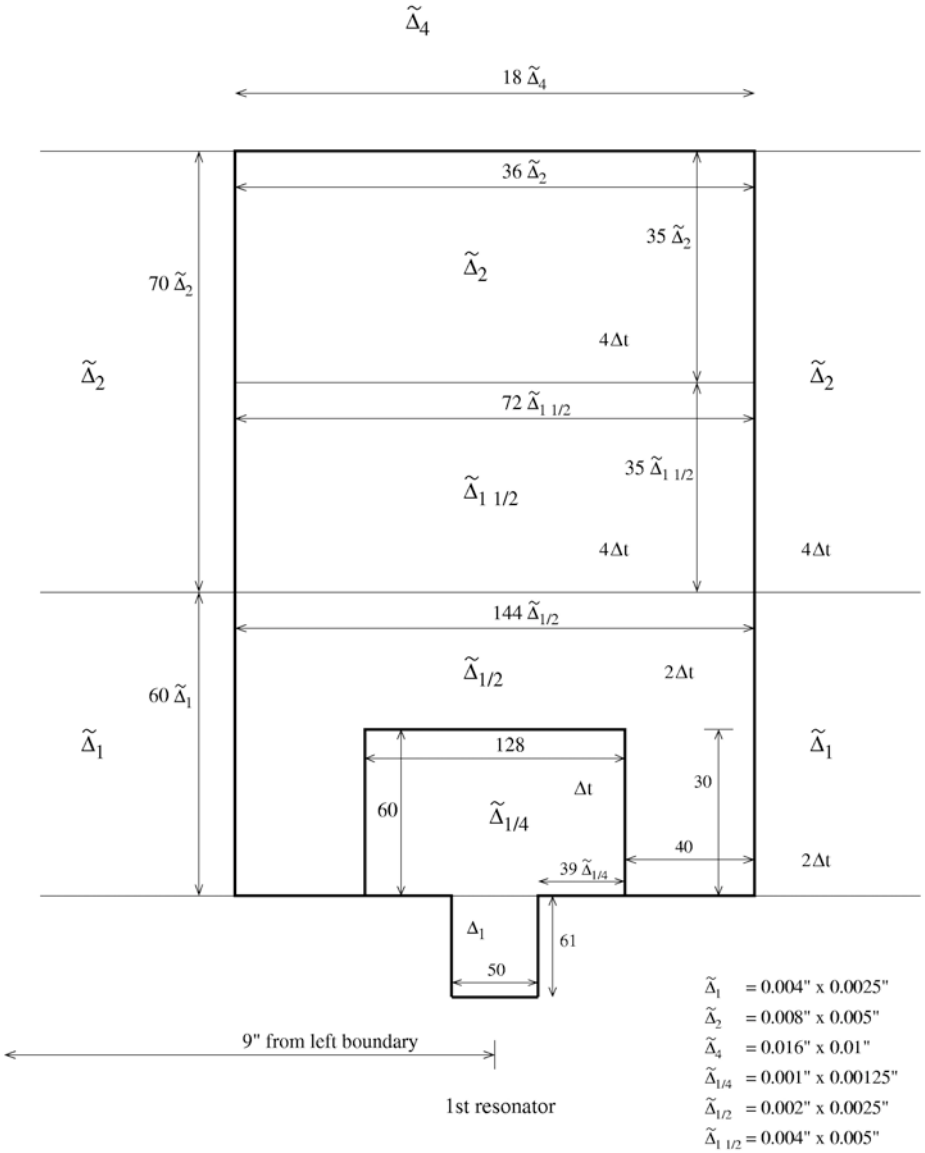

Figure 5. Mesh sizes and mesh distribution just above the opening of a resonator.

Fig. 5 shows the grid design just above the opening of a resonator. This design aims to keep the mesh size increase between adjacent computational subdomain to a factor of two or less. This design leads to a slight increase in the number of mesh points. The finest mesh is in the resonator opening. The mesh size is chosen so that it can provide adequate resolution of the Stokes layer adjacent to the walls of the opening at 3 kHz.

Fig. 6 shows the mesh size distribution inside a resonator. The number of mesh points is 73,820. There are 8 resonators. So, the total number of mesh points inside the resonators is approximately 600,000. Therefore, the total number of mesh points used in the present grazing flow tube simulation is around 1.7 million.

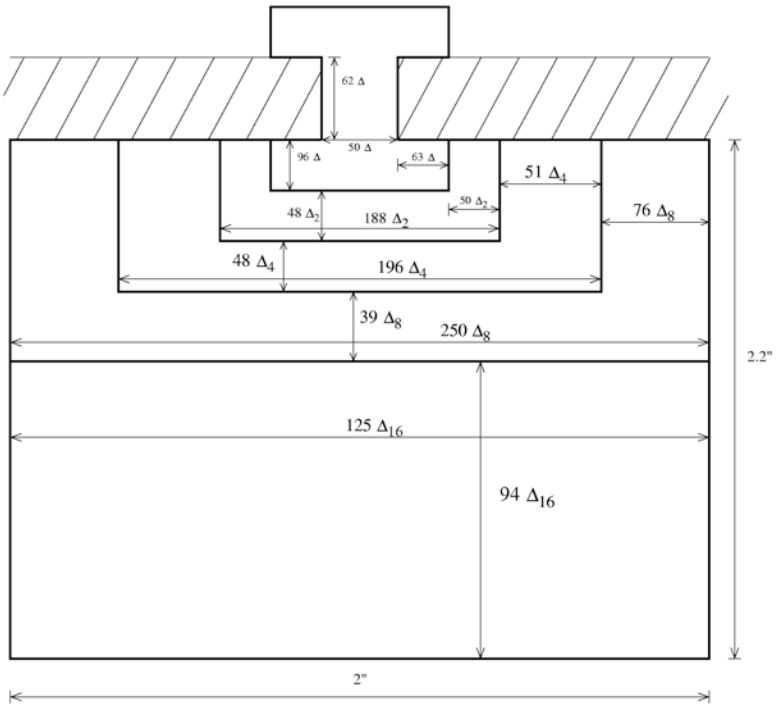

Figure 6. Mesh size and mesh distribution inside a typical resonator. $\Delta = 0.001$ in. $\Delta_n = n\Delta$.

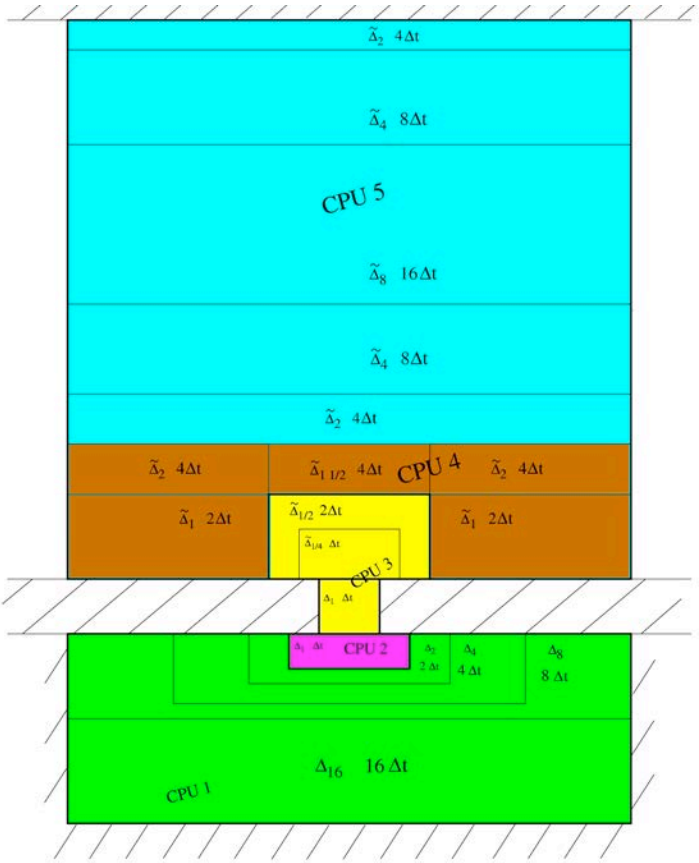

Figure 7. Assignment of cores/CPUs to different parts of the computational domain inside and outside a resonator.

The computer code used in this investigation is a parallel code. Fig. 7 shows the cores/CPUs assigned to perform the computation for the different computational subdomains. The most intense computation takes place around the openings of the resonators. As a result, more cores/CPUs are assigned to these regions. Overall, 56 cores/CPUs are used by the computer code. Fig. 8 shows the allocation of computational subdomain to each of the 56 cores. The design is intended to distribute the computational load evenly to each core.

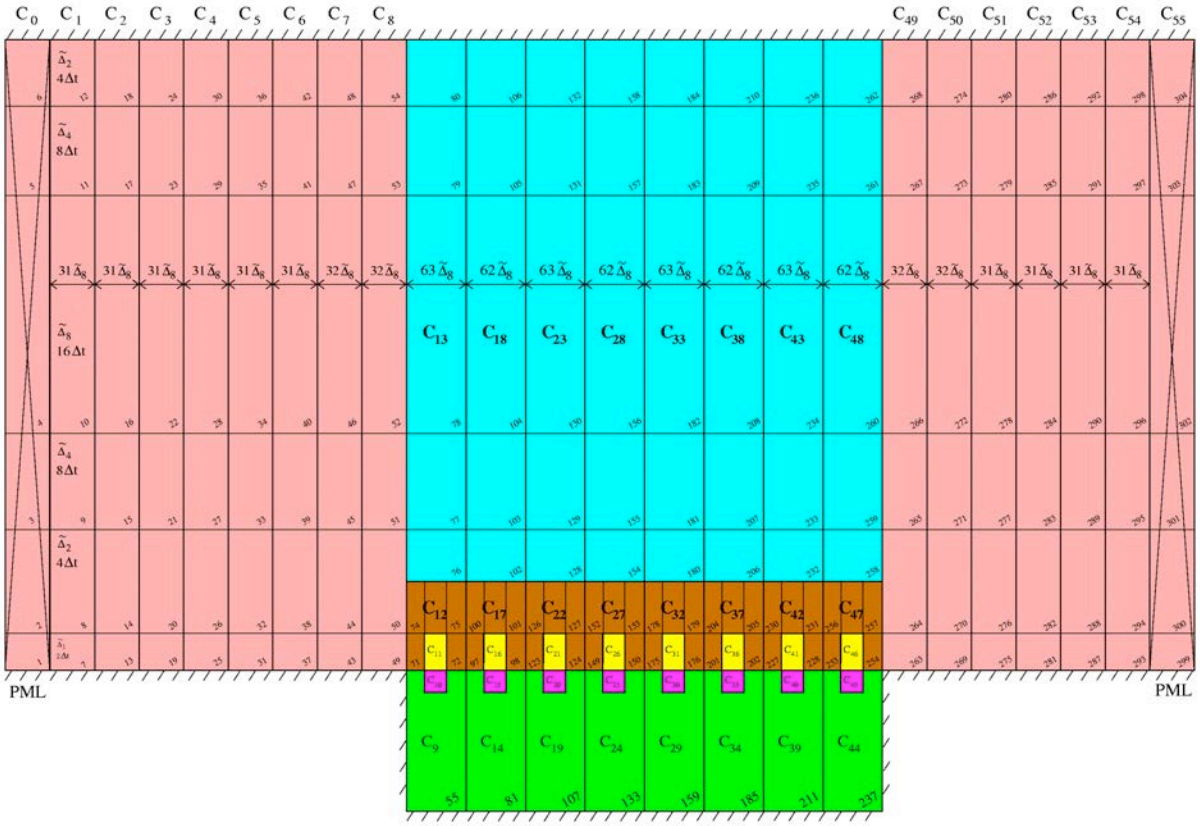

Figure 8. Assignment of computational subdomain to each of the 56 cores of the computer code.

3.2 Governing Equations

In this project, a two dimensional model is used. The turbulent mean flow is computed using a turbulent eddy viscosity model (see Appendix A). Basically, the governing equations are the Reynolds averaged Navier-Stokes equations (RANS) with a turbulent eddy viscosity $\nu_T(y)$. Dimensionless variables with respect to the following scales are used.

Length scale = H (the height of the channel = 2.5 inches)
Velocity scale = a_0 (speed of sound)
Time scale = H / a_0
Density scale = ρ_0 (inflow gas density)
Pressure scale = $\rho_0 a_0^2$
Viscosity scale = Ha_0
Stress scale (see definition of σ) = a_0^2

The RANS equations are,

$$\frac{\partial \rho}{\partial t} + u\frac{\partial \rho}{\partial x} + v\frac{\partial \rho}{\partial y} + \rho\left(\frac{\partial u}{\partial x} + \frac{\partial v}{\partial y}\right) = 0 \tag{1}$$

$$\frac{\partial u}{\partial t} + u\frac{\partial u}{\partial x} + v\frac{\partial u}{\partial y} = -\frac{1}{\rho}\frac{\partial p}{\partial x} + \frac{\partial \sigma_{xx}}{\partial x} + \frac{\partial \sigma_{xy}}{\partial y} \tag{2}$$

$$\frac{\partial v}{\partial t} + u\frac{\partial v}{\partial x} + v\frac{\partial v}{\partial y} = -\frac{1}{\rho}\frac{\partial p}{\partial y} + \frac{\partial \sigma_{yx}}{\partial x} + \frac{\partial \sigma_{yy}}{\partial y} \tag{3}$$

$$\frac{\partial p}{\partial t} + u\frac{\partial p}{\partial x} + v\frac{\partial p}{\partial y} + \gamma p\left(\frac{\partial u}{\partial x} + \frac{\partial v}{\partial y}\right) = 0 \tag{4}$$

$$\sigma_{xx} = 2\left(\frac{1}{R_T} + \frac{1}{R}\right)\frac{\partial u}{\partial x}, \quad \sigma_{yy} = 2\left(\frac{1}{R_T} + \frac{1}{R}\right)\frac{\partial v}{\partial y} \tag{5}$$

$$\sigma_{xy} = \sigma_{yx} = \left(\frac{1}{R_T} + \frac{1}{R}\right)\left(\frac{\partial u}{\partial y} + \frac{\partial v}{\partial x}\right) \tag{6}$$

where $R_T = \dfrac{1}{\nu_T}$ and $R = \dfrac{1}{\nu}$ are the turbulent and molecular Reynolds numbers and $\nu_T(y)$ is determined in Appendix A.

Inside a channel, the turbulent flow is resisted by the shear stresses at the walls. To maintain the flow, a pressure gradient must be applied. To simulate such flows, the pressure imposed on the inflow and outflow surfaces of the computational domain will not be the same. The imposition of a fixed pressure at a boundary will prevent the passage of acoustic disturbances through that boundary. Thus from a computational aeroacoustics standpoint, imposing a pressure boundary condition on both ends of a channel would lead to extremely undesirable consequences. Acoustic disturbances will be trapped inside the channel with no escape route. They will have to be dissipated by the inclusion of artificial damping. However, too much damping should always be avoided in aeroacoustic computation. To circumvent this problem, a pressure gradient transformation is adopted in this work. Suppose the mean pressure at the inflow surface, $x = x_1$, is $p = p_1$ and that at the outflow surface, $x = x_2$, is $p = p_2$, the pressure gradient may be incorporated in an auxiliary variable, P, as follows

$$\text{Let } P = p_1 - \frac{p_1 - p_2}{x_2 - x_1}\left(x - x_1\right) = p_1 - \bar{\beta}\left(x - x_1\right) = \frac{1}{\gamma} - \bar{\beta}\left(x - x_1\right) \tag{7}$$

where $\dfrac{dP}{dx} = -\bar{\beta}$

The balance between wall stresses and mean flow pressure gradient in a parallel flow leads to the condition (see Eq. (A4) in Appendix A),

$$\bar{\beta} = 2\left(\nu^*\right)^2 \tag{8}$$

where ν^* is the friction velocity of a turbulent boundary layer.

On introducing $p = P + p'$ into governing Eqs (1) to (6), only Eqs. (2) - (4) are altered. All the other equations remain the same. To a good degree of approximation for low Mach number flow, Eqs. (2) - (4) become,

$$\frac{\partial u}{\partial t}+u\frac{\partial u}{\partial x}+v\frac{\partial u}{\partial y}=-\frac{1}{\rho}\frac{\partial p'}{\partial x}+\frac{\partial \sigma_{xx}}{\partial x}+\frac{\partial \sigma_{xy}}{\partial y}+\bar{\beta} \tag{9}$$

$$\frac{\partial v}{\partial t}+u\frac{\partial v}{\partial x}+v\frac{\partial v}{\partial y}=-\frac{1}{\rho}\frac{\partial p'}{\partial y}+\frac{\partial \sigma_{yx}}{\partial x}+\frac{\partial \sigma_{yy}}{\partial y} \tag{10}$$

$$\frac{\partial p'}{\partial t}+u\frac{\partial p'}{\partial x}-\bar{\beta}u+v\frac{\partial p'}{\partial y}+\gamma\left(p'+P\right)\left(\frac{\partial u}{\partial x}+\frac{\partial v}{\partial y}\right)=0 \tag{11}$$

In Appendix A, it is determined that the eddy viscosity distribution across the Grazing Flow Impedance Tube is approximately given by (Eq. (A9)),

$$\nu_T=\frac{\bar{\beta}}{\Gamma \nu*}y(1-y)=\frac{2\nu*}{\Gamma}y(1-y) \tag{12}$$

The numerical values of Γ and $\nu*$ for the NASA Grazing Flow Impedance Tube are,

$$\Gamma = 7.752,\ \ \nu*(\text{dimensional}) = 3.6803\ m/s;\ \ \nu*(\text{dimensionless}) = 0.010824$$

3.3 Mean Flow Computation

The entire computation is carried in two steps. First is the mean flow computation. The second step is the acoustic computation. The reason for using a two-step computation instead of a single computation is that different boundary conditions are required for the mean flow and the sound field.

For mean flow computation, one requirement is to use the measured mean flow of the NASA Langley Grazing Flow Impedance Tube as an inflow boundary condition, i.e.

$$\begin{bmatrix}\bar{\rho}\\ \bar{u}\\ \bar{v}\\ \bar{p}'\end{bmatrix}=\begin{bmatrix}1\\ \hat{u}(y)\\ 0\\ 0\end{bmatrix} \tag{13}$$

where $\hat{u}(y)$ is the velocity profile given by Eq. (A10) of Appendix A (see Fig. A1).

The outflow is expected to differ slightly from that of the inflow. To allow for this possibility, a split-variable method is used (see Ref. [25] Chapter 9, Section 9.1). In the outflow region (see Fig. 3) the flow variables are divided into two parts as,

$$\begin{bmatrix}\bar{\rho}\\ \bar{u}\\ \bar{v}\\ \bar{p}'\end{bmatrix}=\begin{bmatrix}1\\ \hat{u}(y)\\ 0\\ 0\end{bmatrix}+\begin{bmatrix}\tilde{\rho}\\ \tilde{u}\\ \tilde{v}\\ \tilde{p}\end{bmatrix} \tag{14}$$

The second part of the right side of Eq. (14) is the possible adjustment of the outflow. It is time dependent. This part is to satisfy the Perfectly Matched Layer (PML) Equations. The PML equations can be found in the paper by Hu[26] (equations (32) and (33)) or in Chapter 9 of Ref. [25].

The governing equations for the mean flow are Eqs. (1), (5), (6), (9), (10) and (11) with all the variables replaced by variables with an over-bar. At the solid surfaces, the no-slip boundary conditions are enforced by the Ghost Point Method of Ref. [27] (see also Chapter 6 of Ref. [25]). The computation is carried out using the multi-size-mesh multi-time-step DRP scheme[24]. To start the computation, Eq. (13) is used inside the grazing flow tube. In the resonators, the starting conditions $\overline{\rho} = 1,\ \overline{u} = 0,\ \overline{v} = 0,\ \overline{p}' = 0$ are used. The time marching computation is continued until a time independent solution (the mean flow) is obtained.

3.4 Acoustic Computation

The acoustic computation uses the same governing equations, grid design and outflow boundary condition as those of the mean flow computation. Only the inflow boundary condition and starting condition are modified. Now the inflow boundary condition includes a grazing incident sound wave (plane wave). To allow for the exit of any reflected waves through the inflow boundary, the split-variable method is again used. The modified inflow boundary condition (see Fig. 9) is,

$$\begin{bmatrix} \rho \\ u \\ v \\ p' \end{bmatrix} = \begin{bmatrix} 1 \\ \hat{u}(y) \\ 0 \\ 0 \end{bmatrix} + A \begin{bmatrix} 1 \\ 1 \\ 0 \\ 1 \end{bmatrix} \cos\left[\left(\frac{x}{1+M} - t\right)\Omega\right] + \begin{bmatrix} \rho' \\ u' \\ v' \\ p'' \end{bmatrix} \tag{15}$$

The known inflow components are the prescribed mean flow (the first term on the right side of Eq. (15)), the incident plane wave (the second term) with amplitude A and angular frequency Ω. These two terms form the first part of the inflow. The second part of the inflow variables is possible reflected or outgoing waves. This component is computed by the PML equations. It is to be noted that a PML models a perfect termination. In the experiment, the downstream termination is slightly reflective for low frequencies. A method to simulate a frequency dependent non-anechoic termination is not available at this time.

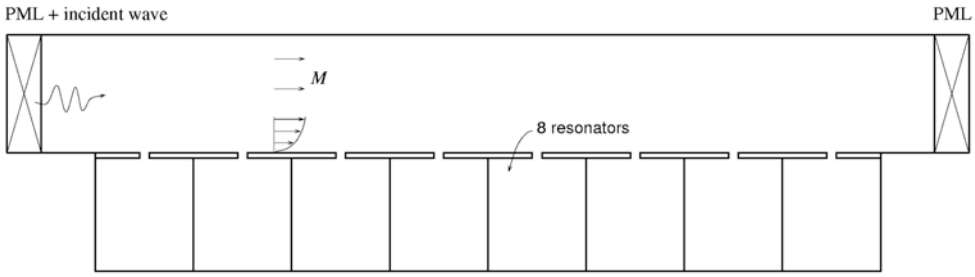

Figure 9. Computational domain showing the inflow and outflow boundary treatments.

The outflow boundary condition is the same as Eq. (14). For the starting conditions the mean flow solution is used throughout the computational domain. In this work, the amplitude of the incident sound wave is turned on gradually. This is done by multiplying the amplitude A of Eq. (15) by the factor $\left(1 - e^{-t/\tau}\right)$. τ is taken to be equal to 5 oscillation periods. The fully nonlinear computation is again carried out by the multi-size-mesh multi-time-step DRP scheme. The time marching computation continues until a time periodic state (numerically speaking) is reached.

The numerical solution obtained consists of the mean flow and the acoustic solution. To find the acoustic component, it is a simple matter to subtract out the mean flow solution at each grid point. This acoustic solution is used to compute numerical results in the following sections. Since the acoustic component is several orders of magnitude smaller than the mean flow, this simple subtraction method requires that the mean flow be computed such that the residuals of the governing equations are exceedingly small. Fortunately, this is not too difficult to do using the method of accelerated convergence developed in Ref. [28] (see also Appendix E of Ref. [25]). In Ref. [28]

an example is provided in which the sound field, generated by a time periodic source, is successfully computed by this method even though it is 10 orders of magnitude smaller than the mean flow.

4. Experimental and Numerical Results

In this section, experimental and numerical results are reported. Numerical results are presented in two parts. Flow results are reported first, and are followed by the acoustic results. At the same time, comparisons between experimental and numerical results are made. This provides valuable validation for the numerical simulation.

4.1 Flow Results

Fig. 10 shows the computed mean velocity profiles at a number of x-locations downstream of the left boundary of the computational domain. Shown in black circles is the original measured profile at the inflow boundary (see Fig. A1 of Appendix A). It is clear from this set of computed results that there is only a small change in the mean velocity over the length of the liner. This is not entirely unexpected since the liner has only a 2.5% opening and has a short length. Typical liners have an open area ratio of about 10% which would induce larger changes in the mean flow.

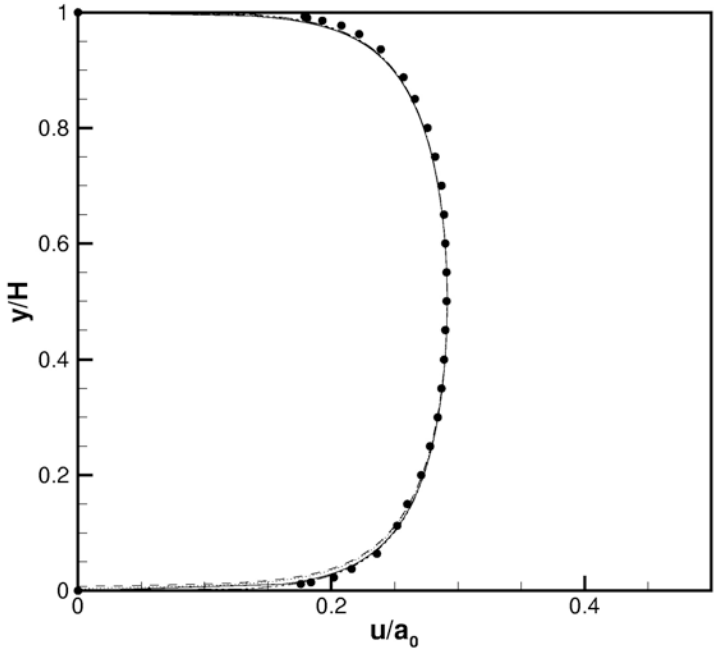

Figure 10 Comparison between computed mean velocity profiles and the measured profile at the inflow boundary.

● measured data
——— profile at the left side of the computational domain
— · · — profile at the right side of the computational domain
– – – – profile at the center of the second cavity
· · · · · · · profile at the center of the seventh cavity

Streamline patterns provide good visualization of circulatory flows. Fig. 11 shows the time averaged streamline pattern of the entire computational domain. Also shown in different colors are sound pressure level contours. Red is high pressure and blue is low pressure. The incident sound has a frequency of 1 kHz at 140 dB SPL entering the computational domain from the left boundary. The computed result indicates that the flow in the channel outside the resonators induces a counterclockwise vortex inside each resonator. The circulation patterns are not identical in each resonator. The vortex flow is not symmetric with respect to the centerline of each resonator. Fig. 12 is an enlarged streamline pattern at the mouth of a resonator. It is evident that because of eddy and molecular

viscosity the outside flow drives a clockwise rotating vortex right at the resonator opening. The vortex, in turn, drives a counterclockwise circulation and vortex flow inside the resonators (seen better in Fig. 13).

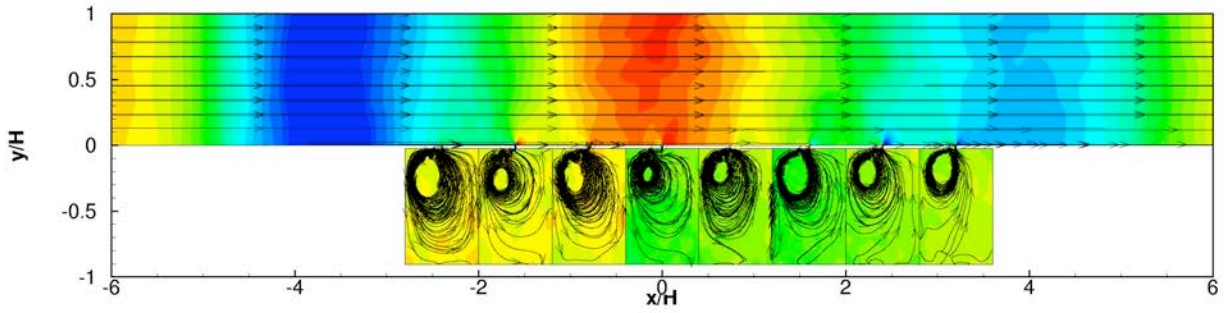

Figure 11. Time averaged streamline pattern in the computational domain. Shown in the background in color are instantaneous sound pressure level contours. Incident sound has a frequency of 1 kHz and a SPL of 140 dB.

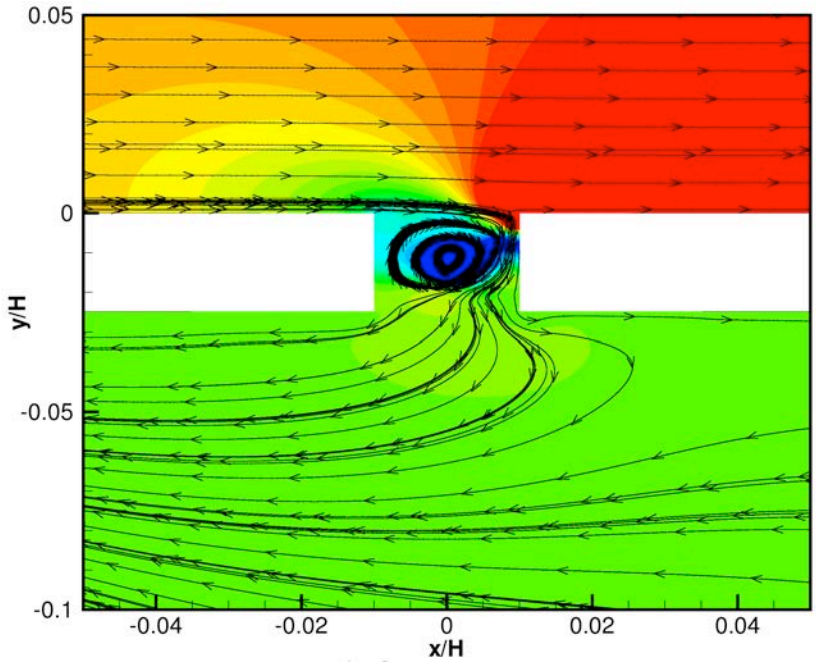

Figure 12 Time averaged streamline pattern displaying the flow-induced circulation at the mouth of a resonator.

Fig. 13 is an enlarged figure of the fourth resonator. It shows more details of the vortical flow inside the resonator. Apparently, there are small vortices embedded in the large circulation at the upper left corner of the resonator cavity. These small vortices are shed from the mouth of the resonator. Vortex shedding is triggered by the incident sound waves.

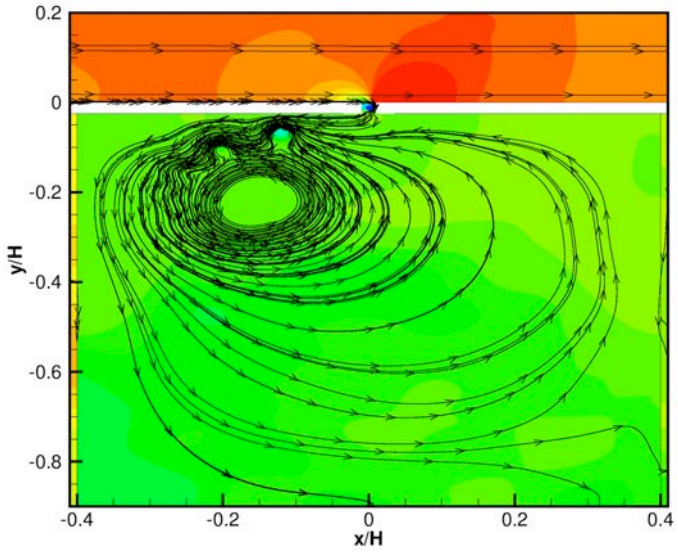

Figure 13 Streamline pattern showing the existence of a circulation flow inside a resonator and small vortices shed from the mouth of the resonator.

On using the standard lumped parameter model, it is easy to find that the resonance frequency of the resonators is around 0.45 kHz. This estimate does not account for the effect of a Mach 0.3 grazing flow. In any case, this suggests that the liner would dissipate more sound waves around 0.5 kHz than, say, at 1.5 kHz or even higher frequencies. Note: the first anti-resonance frequency of the resonators is at 2.68 kHz. An effective way of dissipating incident sound is through vortex shedding. Earlier, Tam and Kurbatskii[11] had suggested that the conversion of acoustic energy into the rotational kinetic energy of the shed vortices is the mechanism for enhanced acoustic dissipation. Fig. 14 shows vortex shedding from the mouths of two neighboring resonators driven by the incident sound. In this figure, shed vortices can be seen both inside and outside the resonators. Our study reveals that vortex shedding is observed only at incident sound frequencies below 1.5 kHz with the strongest shedding at 0.5 kHz (the lowest frequency of our simulation effort). This is the frequency closest to the resonator resonance frequency. It will be shown later that strong vortex shedding correlates well with the magnitude of the rate of sound absorption by the acoustic liner. When there is no vortex shedding, the sound absorption rate is minimal.

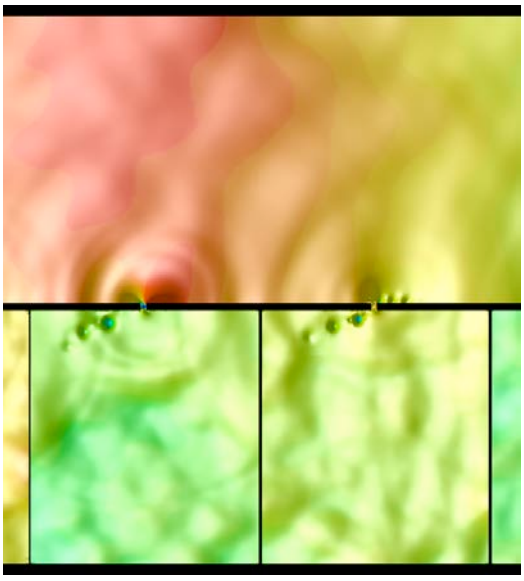

Figure 14. Enlarged picture of the acoustic field in two neighboring resonators. Shown also are the shed vortices inside and outside the resonators. Frequency of incident sound is 1 kHz.

4.2 Acoustic Results

In the NASA experiment, an array of microphones is mounted on the wall opposite the liner. The signals measured by these microphones provide information about the streamwise distribution of sound pressure level (SPL) and phases relative to the incident sound. The distribution of SPL and phases provide information on the interaction of the incident sound and the acoustic liner.

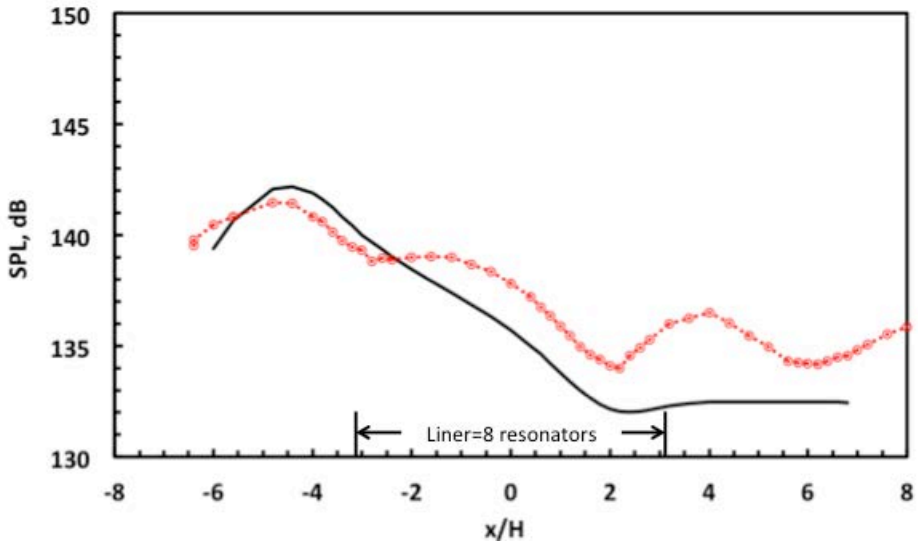

Figure 15. Streamwise distribution of SPL along the wall opposite the liner. Mean flow at Mach 0.3. Incident sound frequency 0.5 kHz and 140 dB SPL. ○ experimental measurement,
——— simulation result.

Fig. 15 shows both the measured and computed SPL distribution on the wall opposite the liner for an incident wave of 140 dB at 0.5 kHz. The solid line is the computed distribution and the circles are the measured data. There is only fair agreement between measured and simulation results. Perhaps the most obvious difference is the presence of a standing wave pattern downstream of the liner trailing edge in the measured data, indicating the presence of a reflective termination in the Grazing Flow Impedance Tube (GFIT) at this frequency. By comparison, the simulation assumes an anechoic termination, and thus exhibits no oscillations in the simulated SPL beyond the near-field of the liner trailing edge. The following brief analysis is provided as support of this conclusion.

Downstream of the liner, the measured data exhibits two prominent peaks. These peaks simply represent the interference pattern of the downstream propagating incident sound wave and that of the reflected wave from the downstream termination of the GFIT. The peak-to-peak distance of the two most downstream peaks or wavelength in Fig. 15 is approximately 12 inches. Both incident and reflected waves have the frequency (0.5 kHz), but the incident wave has a wave speed equal to the speed of sound plus the mean flow velocity $\left(\bar{a}+\bar{u}\right)$. The reflected wave, however, has a wave speed equal to the speed of sound minus the mean flow velocity i.e. $\left(\bar{a}-\bar{u}\right)$; it being propagating against a Mach 0.3 flow. Suppose the pressure amplitude of the waves are A and B respectively and their relative phase is ϕ. Then the pressure in the Grazing Flow Impedance Tube is the sum of the pressures of the two waves,

$$p = A\cos\left[\omega\left(\frac{x}{\bar{a}+\bar{u}}-t\right)\right] + B\cos\left[\omega\left(\frac{x}{\bar{a}-\bar{u}}+t\right)+\phi\right] \qquad (16)$$

It is easy to show that the time averaged squared pressure is,

$$\overline{p^2} = \tfrac{1}{2}\left(A^2 + B^2\right) + AB\cos\left[\frac{2\bar{a}\omega x}{\bar{a}^2 - \bar{u}^2} + \phi\right] \tag{17}$$

The last term of Eq. (17) is responsible for the exhibition of spatial oscillation of $\overline{p^2}$. The wavelength λ, from the cosine term, is

$$\lambda = \frac{\pi\left(\bar{a}^2 - \bar{u}^2\right)}{\bar{a}\omega} \tag{18}$$

On taking the speed of sound to be 340 m/s, it is straightforward to find $\lambda = 12.18$ inches. This matches well with the measured wavelength (peak to peak distance) of approximately 12 inches. Thus the difference between the computed results and the measured data is at least partially due to the reflective termination of the experimental facility at this frequency. As the frequency is increased from 0.5 kHz to 2.0 kHz, the GFIT termination approaches an anechoic condition. Thus better agreement between measured and simulated results should be achieved for higher frequencies.

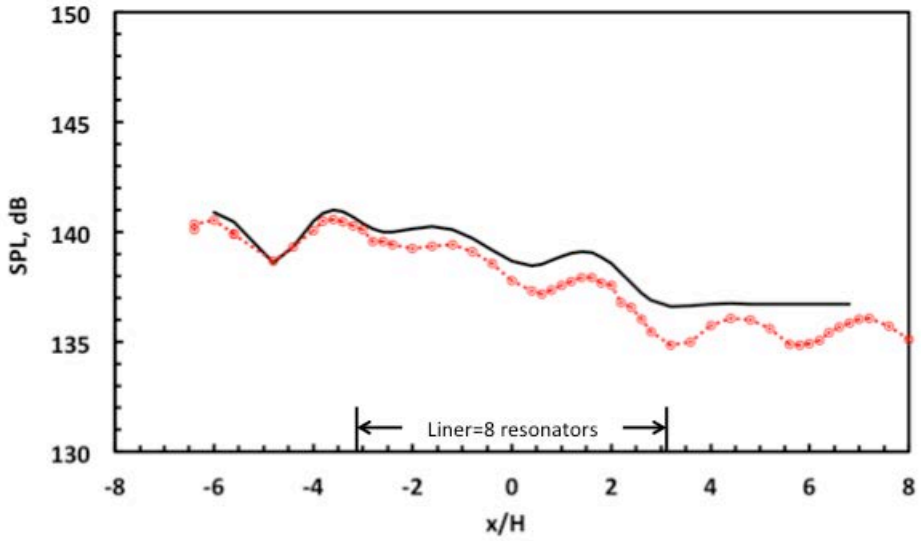

Figure 16. Streamwise distribution of SPL along the wall opposite the liner. Mean flow at Mach 0.3. Incident sound frequency 1.0 kHz and 140 dB SPL. O experimental measurement,
——— simulation result.

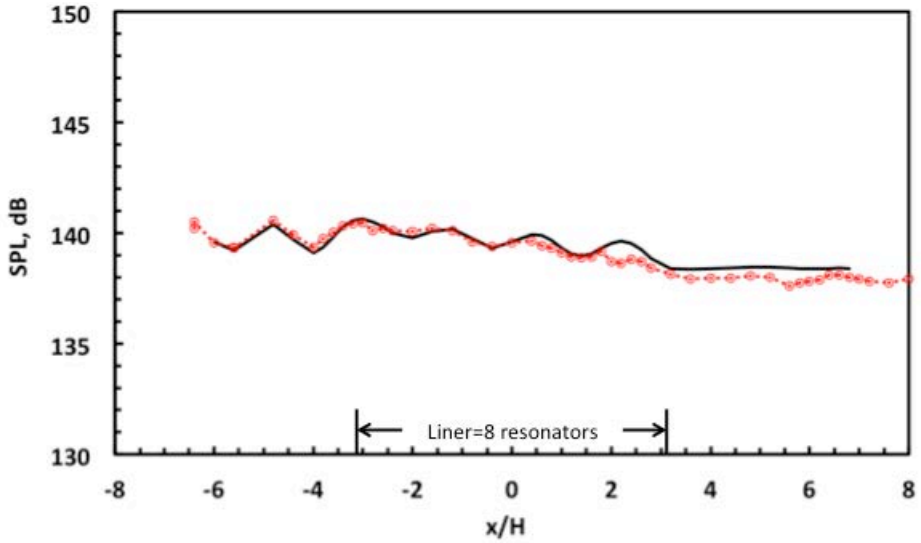

Figure 17. Streamwise distribution of SPL along the wall opposite the liner. Mean flow at Mach 0.3. Incident sound frequency 1.5 kHz and 140 dB SPL. O experimental measurement, ——— simulation result.

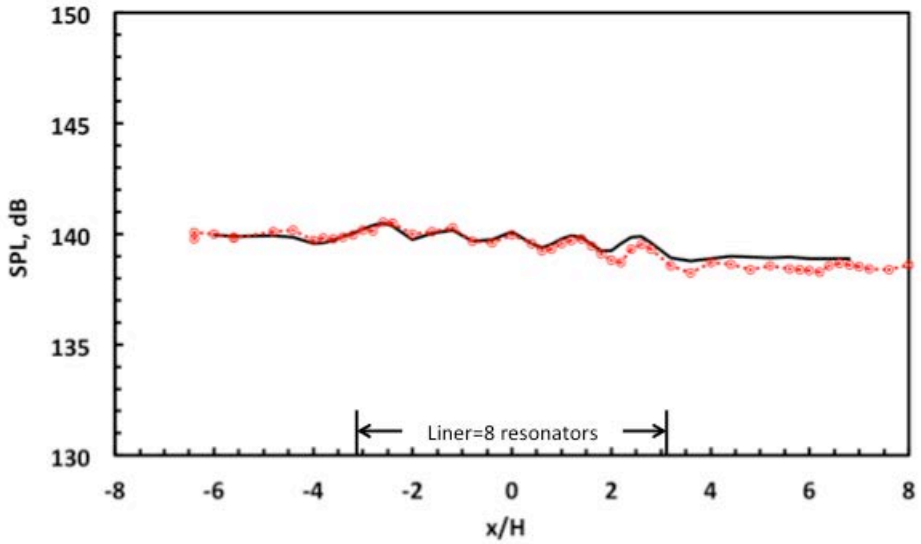

Figure 18. Streamwise distribution of SPL along the wall opposite the liner. Mean flow at Mach 0.3. Incident sound frequency 2.0 kHz and 140 dB SPL. O experimental measurement,
——— simulation result.

Figs. 16, 17, 18 show similar comparisons as Fig. 15. The SPL of the incident sound wave is kept at 140 dB. The frequencies are at 1.0, 1.5, 2.0 kHz. It is clear from these figures that the agreement between computed and measured spatial distribution of SPL improves as frequency increases. At 2 kHz the agreement is excellent.

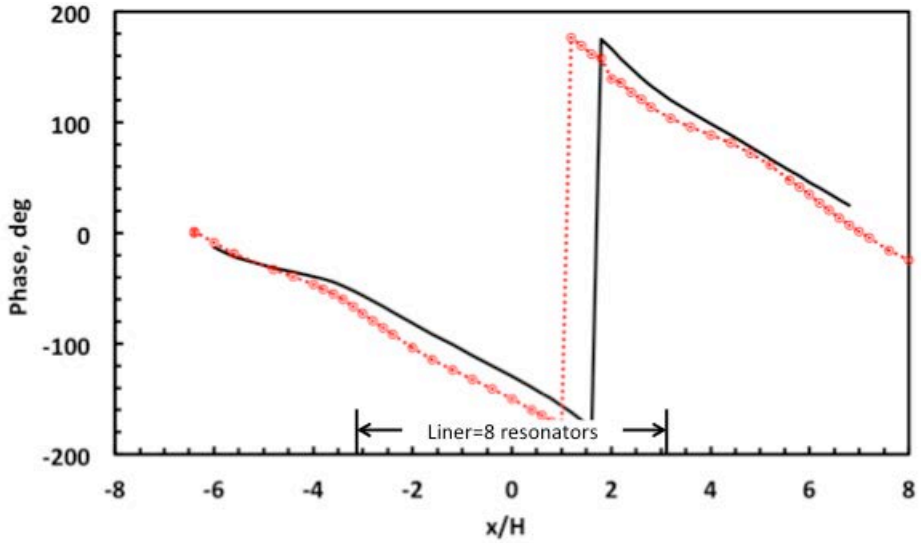

Figure 19. Streamwise distribution of relative phase along the wall opposite the liner. Mean flow at Mach 0.3. Incident sound frequency 0.5 kHz and 140 dB SPL. O experimental measurement, ——— simulation result.

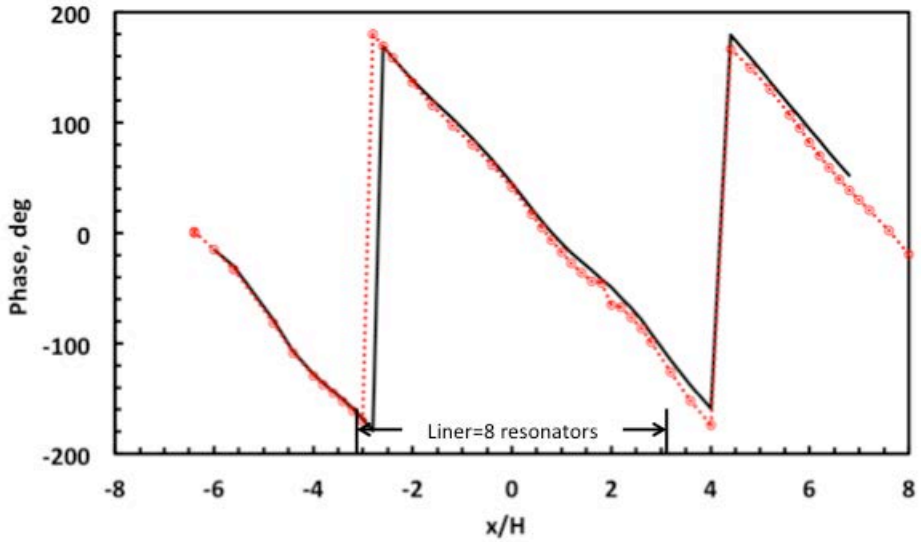

Figure 20. Streamwise distribution of relative phase along the wall opposite the liner. Mean flow at Mach 0.3. Incident sound frequency 1.0 kHz and 140 dB SPL. O experimental measurement, ——— simulation result.

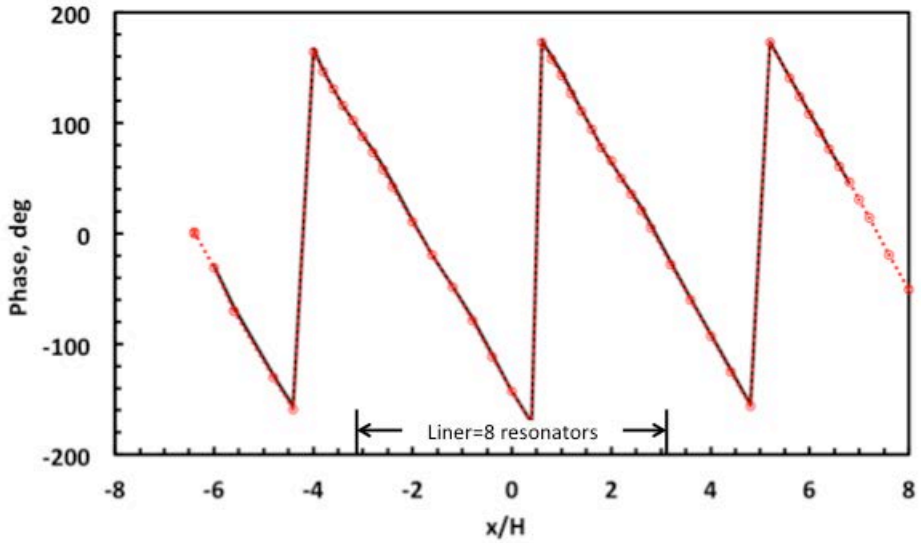

Figure 21. Streamwise distribution of relative phase along the wall opposite the liner. Mean flow at Mach 0.3. Incident sound frequency 1.5 kHz and 140 dB SPL. O experimental measurement, ——— simulation result.

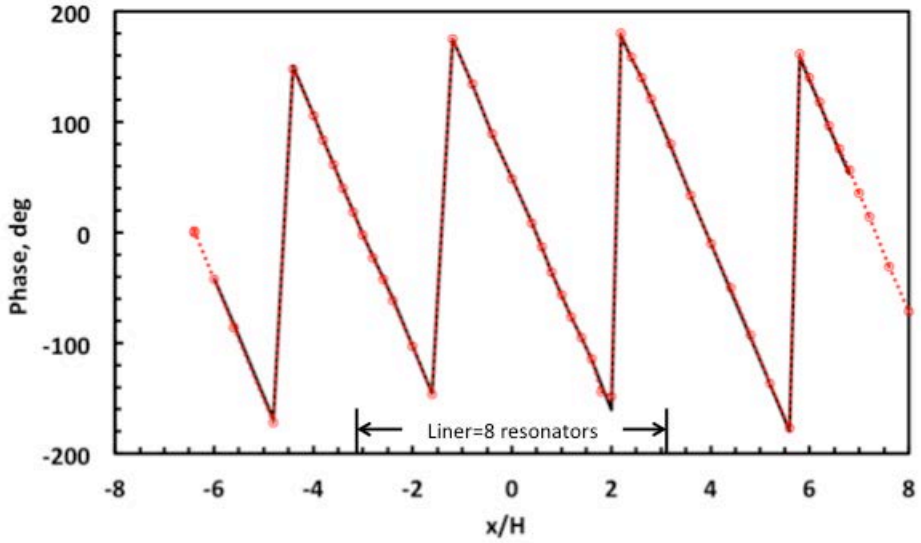

Figure 22. Streamwise distribution of relative phase along the wall opposite the liner. Mean flow at Mach 0.3. Incident sound frequency 2.0 kHz and 140 dB SPL. O experimental measurement, ——— simulation result.

Figs.19 to 22 show comparisons of the spatial distribution of the relative phase of the computed and measured data. The agreements are good for all cases considered.

To provide additional validation of the simulation code, an extra run at 2 kHz but at a higher SPL, (SPL=148.6 dB) was measured and computed. Fig. 23 shows the comparison of the spatial distribution of SPL along the duct wall opposite the liner. It is evident that there is good agreement. Fig. 24 shows the comparison of the phase distribution. There is again good agreement. Based on all the above comparisons, we are of the opinion that the numerical simulation code has been validated as well as can be expected, given the fact that the GFIT termination is slightly reflective while the numerical simulation assumes an anechoic termination.

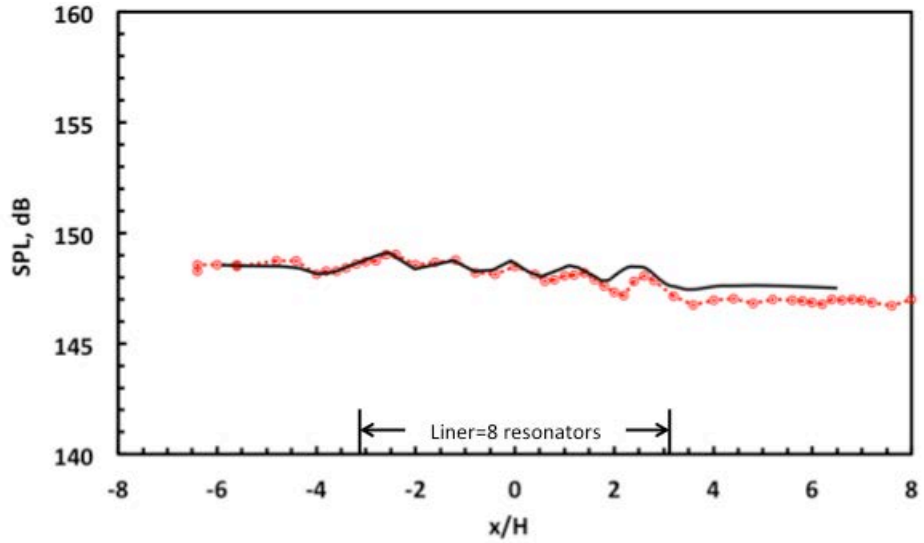

Figure 23. Streamwise distribution of SPL along the wall opposite the liner. Mean flow at Mach 0.3. Incident sound frequency 2.0 kHz and 148.6 dB SPL. O experimental measurement, ——— simulation result.

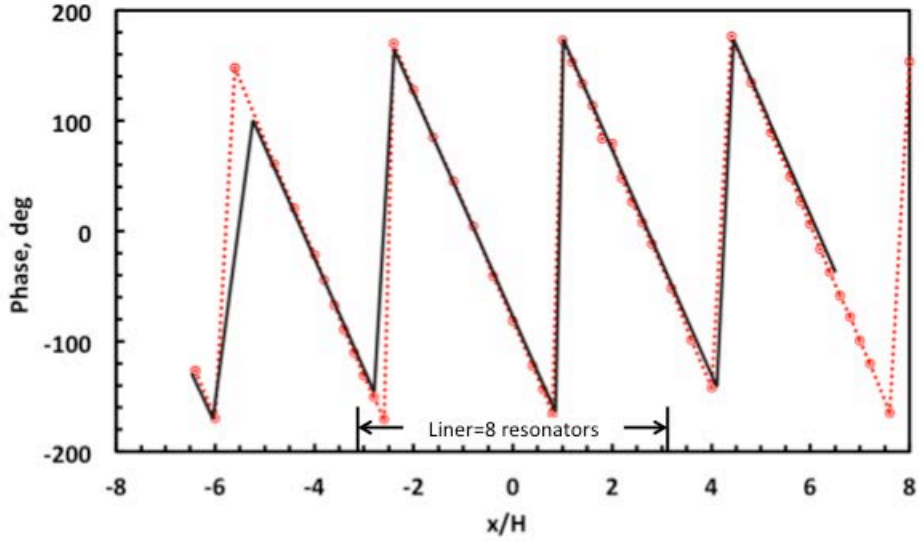

Figure 24. Streamwise distribution of relative phase along the wall opposite the liner. Mean flow at Mach 0.3. Incident sound frequency 2.0 kHz and 148.6 dB SPL. O experimental measurement, ——— simulation result.

5. Liner Self-Noise and Added Drag

5.1 Self-noise

The purpose of installing an acoustic liner in a jet engine inlet is to absorb sound waves. However, in the present study, we found, through numerical simulation, that an acoustic liner could also produce self-noise. Fortunately, the frequency of the observed self-noise is very high, beyond normal hearing range.

Fig. 25 shows the instantaneous sound field (pressure level contours) in the whole computational domain for an incident plane wave at 1 kHz frequency and 140 dB SPL. In this figure, red color indicates high pressure. Blue color indicates low pressure. At 1 kHz, the wavelength of the incident sound is almost the same as the length of the liner (8 resonators). Superimposed on this acoustic field are high frequency waves with short wavelengths. There

is a large disparity between the wavelength of the 1 kHz wave and the high frequency waves so that the existence of the high frequency waves is clear. This high frequency radiation is evident both in the flow duct and in the resonators. The high frequency waves appear to be emitted at the mouths of the resonators. Part of the waves radiate out into the grazing flow tube and part of the waves radiate into the resonators. On reflection at solid surfaces, the high frequency waves form a very complex pattern.

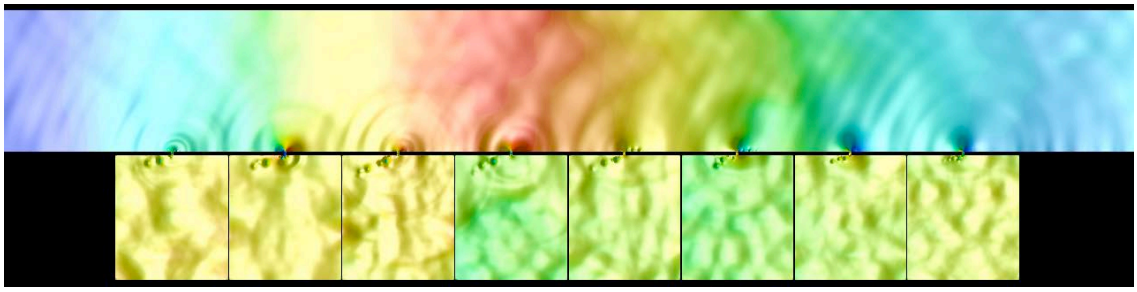

Figure 25. Instantaneous acoustic field inside the entire computational domain. High frequency sound waves (self-noise) are emitted from the mouths of resonators. Frequency of incident sound is 1 kHz.

Fig. 26 shows a similar acoustic field at an incident sound frequency of 2.5 kHz and a SPL of 140 dB. At this frequency, there is a diminished vortex shedding activity as compared to cases at lower incident sound wave frequencies. In this figure, the high frequency waves form a near regular pattern inside the resonators. On the other hand, inside the grazing flow tube, the incident sound waves retain a plane wave-like wave-front quite unlike that when the frequency of the incident wave is 1 kHz (Fig. 25).

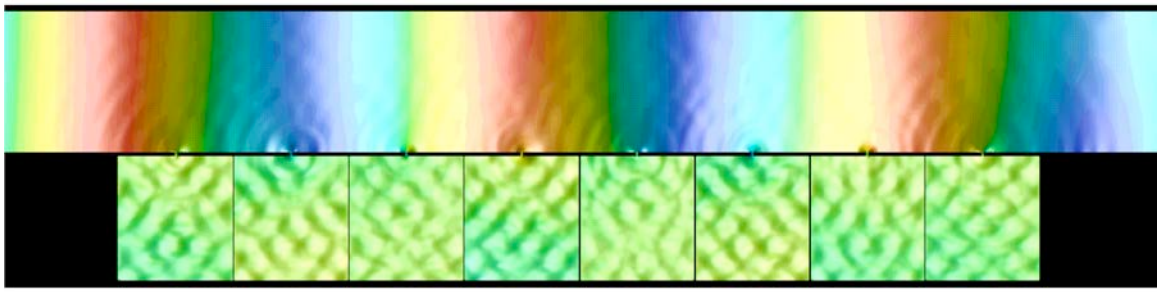

Figure 26. Instantaneous acoustic field inside the entire computational domain. High frequency sound waves (self-noise) are emitted from the mouths of resonators. Frequency of incident sound is 2.5 kHz.

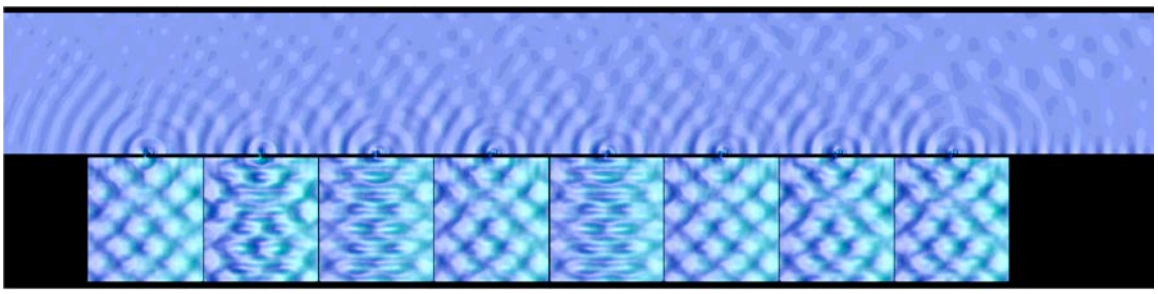

Figure 27. Instantaneous acoustic field inside the entire computational domain. High frequency sound waves (self-noise) are emitted from the mouths of resonators. There is no incident sound.

In both Figs. 25 and 26 the wavelengths of the high frequency waves appears to be nearly the same. Since the wavelengths of the incident sound waves are quite different, it appears that the high frequency waves might not be related to the incident wave. To be sure that these waves are, indeed, liner self-noise, totally unrelated to the incident sound waves, a simulation was carried out with only the mean flow and without incident sound. Fig. 27

shows the computed sound field at a particular instant over the entire computational domain. Clearly, the high frequency sound waves are easily observable proving that it is generated by the interaction of the mean flow and the liner. It is, therefore, a liner self-noise.

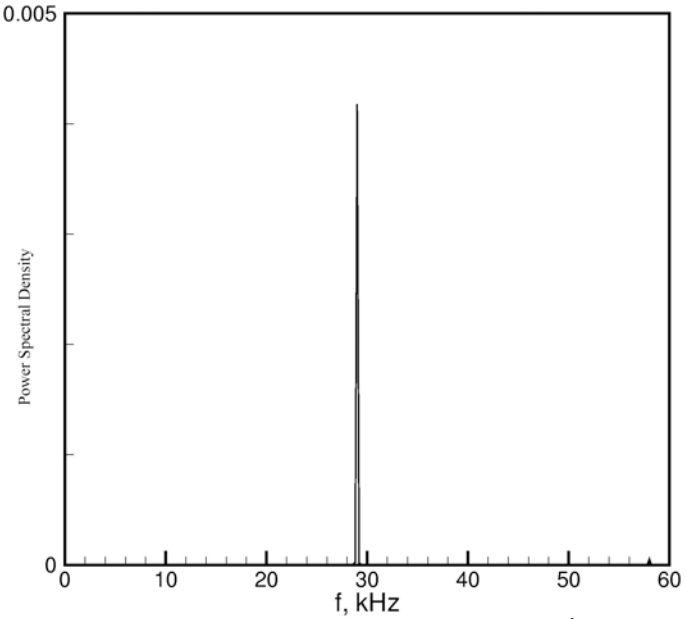

Fig. 28. Liner self-noise spectrum computed on the wall opposite the 4th resonator of the liner.

Fig. 28 shows the spectrum of the liner self-noise computed at the point on the wall opposite to the center of the 4th resonator of the liner. The spectrum consists essentially of a sharp spike at 29 kHz. Noise spectra measured at other locations confirm that the noise is a tone at a frequency of 29 kHz. The tone intensity, however, varies from place to place. Table 1 provides the intensity of the tone at the specified locations.

Table 1. Intensity of liner self-noise tone

Location of simulation, (*x, y*)	SPL of tone in dB
(4.5, 0.13)	95.5
(-1.6, -0.465)	107.5
(-1.3, -0.1)	105.4
(0.0, 1.0)	93.5
(-3.0, 0.28)	91.0

Note: (*x,y*) are dimensionless; length scale = *H* (2.5 inches). The origin of the coordinate system is on the face sheet at the center of the 4th resonator.

Generally speaking, the self-noise is most intense inside the resonators. The SPL can reach up to 107.5 dB. The SPL in the Grazing Flow Impedance Tube is in the range of 90 to 95 dB. In the inlet of a jet engine, the sound

pressure intensity can reach a level of 150 dB. Thus, on a relative basis, the intensity of liner self-noise is quite negligible, at least for the liner considered in the current investigation.

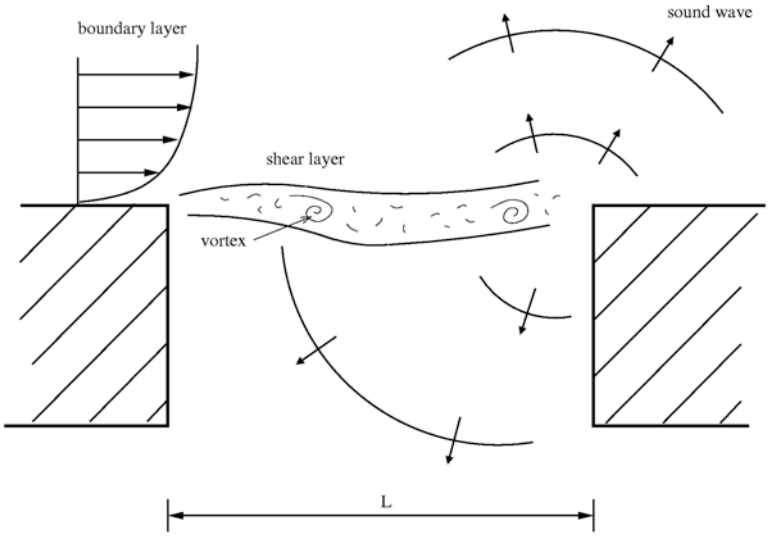

Figure 29. Feedback resonance loop at the mouth of a resonator.

A closer examination of the simulation data reveals that the self-noise tone is generated by a feedback loop as shown in Fig. 29 (see also Heller[29] and Kegerise[30]). Spanning over the opening mouth of a resonator is a thin shear layer. The thin shear layer is unstable due to Kelvin-Helmholtz instability. The Kelvin-Helmholtz instability wave is excited near the leading edge of the resonator opening. The excited instability wave grows rapidly in amplitude as it propagates downstream. When the amplitude becomes large the instability wave rolls up to form a vortex-like structure. The vortex structure moves downstream supported by the mean flow. Eventually, it strikes the trailing edge of the resonator opening. The impact creates an acoustic pulse. Part of the pulse propagates upstream inside the mouth of the resonator. When this sound pulse reaches and impinges on the leading edge of the resonator opening it generate a disturbance that excites the thin shear layer. This excitation creates a new instability wave. In this way, the feedback loop is closed.

According to the above feedback model, the travel time for the vortex structure to go from the leading edge of the resonator opening to the trailing edge plus the time needed for the sound wave to propagate from the trailing edge to the leading edge must be equal to n times the period of the self-noise tone. That is, if T is the period of the tone, u_c is the vortex structure convection velocity, a_0 is the speed of sound and L is the width of the resonator opening, then,

$$nT = \frac{L}{u_c} + \frac{L}{a_0}. \tag{18}$$

Therefore,

$$\frac{u_c}{a} = \frac{1}{\frac{nTa_0}{L} + 1} \tag{19}$$

On taking $a_0 = 340 m/s$, $L = 0.05$ inches, $T = \frac{1}{f} = \frac{1}{29{,}000}$ sec. and $n = 2$ (there are two vortices in the shear layer), it is easy to find by means of Eq. (19) that $\frac{u_c}{a_0} = 0.0563$. The averaged value of $\frac{u_c}{a_0}$ measured from numerical simulation data is 0.0556. This is very close to the computed value based on the feedback loop. We regard the good agreement as strong evidence that the self-noise tone is, indeed, a consequence of feedback resonance.

5.2 Liner Drag

The continuous impingement of the vortices in the shear layer spanning the resonator opening of a liner on the trailing edge of the resonator opening results in a drag force on the liner. Although the momentum carried by each tiny vortex is small, the frequency of impact is huge resulting in increased drag. To quantify the drag, let D be the average diameter of the vortices. The momentum, m, of each vortex is,

$$m = \tfrac{1}{4}\pi D^2 \rho u_c \tag{20}$$

The total force created by impact on the trailing edge is,

$$F = \tfrac{1}{4}\pi D^2 \rho u_c f \tag{21}$$

This is the drag force on a resonator. Thus, if W is the width of a resonator, the equivalent shear stress per unit width of the face sheet, τ is equal to,

$$\tau = \frac{F}{W} = \frac{\pi D^2 \rho u_c f}{4W} \tag{22}$$

For a mean flow of Mach 0.3 in the NASA Grazing Flow Impedance Tube, it is found in Appendix A that the shear stress, τ_w, exerted on a solid wall by a turbulent boundary layer is equal to $\rho\left(v^*\right)^2$ where $v^* = 3.68$ *m/s*. The averaged value of D measured from the simulation data is $D \simeq 0.005$ inches. Hence, by Eq. (22), it is found,

$$\frac{\tau}{\tau_w} = 0.0102 .$$

That is, the liner drag created by acoustic resonance is approximately 1% of the standard turbulent boundary layer drag. However, the open area ratio of the liner used in the present investigation is 2.5%. For a standard liner, it is about 10%. That is to say, for the same open area ratio as that of a standard liner, the additional liner drag is 4% of the turbulent boundary layer drag for a flat wall. It should be noted that a 4% added drag is not a trivial matter from an aerodynamic point of view.

6. Conclusion

In this investigation, experimental measurements and numerical simulations of an acoustic liner in a grazing flow are performed. This is one of the first, if not the very first, simulation effort for a multi-resonator liner mounted in a grazing flow duct. A parallel experimental study was carried out at the NASA Langley Research Center. The aim is to provide experimental validation of the computer code developed as a part of this investigation. On comparing the computed results and experimental measurements, good agreements are found. This provides confidence in the accuracy of the simulation code. It is believed that the present effort represents an important step forward in the application of CAA methods to acoustic liner technology.

As a part of the present investigation, it is found that an acoustic liner can generate self-noise. Fortunately, for the liner under study, the self-noise consists of a tone at a very high frequency; beyond the normal hearing range. The tone appears to be a feedback resonance phenomenon. The feedback loop is driven by the Kelvin-Helmholtz instability wave of the free shear layer spanning the openings of the resonators of the liner. Observations of the simulated flow field show that the shear layer instability wave rolls up to form vortex-like structures. These vortices impinge on the trailing edges of the resonator openings producing a tone as well as creating a drag on the liner.

Based on a vortex momentum impact calculation, it is estimated that for a liner with a 10% open area, the added drag would be approximately 4% of the turbulent boundary layer drag for a flat wall. This is not a negligible additional drag. Thus, it appears that it might be worthwhile to modify slightly the design of the openings of the resonators of a liner so as to minimize flow resonance and hence added liner drag.

Appendix A. Mean Velocity Profile and Eddy Viscosity Distribution in the NASA Grazing Flow Impedance Tube.

In this Appendix, formulas for the turbulent mean velocity profile and eddy viscosity distribution inside a long channel are developed. One principal assumption is that the effect of turbulence on the mean flow can be modeled by the use of an eddy viscosity ν_T . In the following, dimensionless variables as defined in Section 3.2 are used.

In a two dimensional channel of height (dimensionless) equal to unity, the x-momentum equation of the Reynolds Averaged Naver-Stokes equations (RANS) with a turbulent eddy viscosity ν_T is (the x-axis forms the lower wall of the channel),

$$\frac{\partial \overline{u}}{\partial t} + \overline{u}\frac{\partial \overline{u}}{\partial x} + \overline{v}\frac{\partial \overline{u}}{\partial y} = -\frac{1}{\overline{\rho}}\frac{\partial \overline{p}}{\partial x} + \frac{\partial}{\partial y}\left[\left(\nu_T + \nu\right)\frac{\partial \overline{u}}{\partial y}\right] \tag{A1}$$

However, for a fully developed turbulent mean flow in a long channel, the mean velocity is parallel to the channel wall or the x-axis. The profile depends only on the lateral coordinate y. That is the mean flow is given by,

$$\overline{u} = \hat{u}(y), \quad \overline{v} = 0.$$

$$\text{Let } \frac{d\overline{p}}{dy} = -\overline{\beta}, \quad (\overline{\beta} \text{ is a constant}, \overline{\beta} \geq 0)$$

Because the mean flow is parallel and steady, Eq. (A1) reduces to ,

$$\frac{d}{dy}\left[\left(\nu_T + \nu\right)\frac{d\overline{u}}{dy}\right] = -\overline{\beta}\,; \quad \left(\overline{\rho} \approx 1\right) \tag{A2}$$

For a wall bounded turbulent flow, if τ_w is the shear stress at the wall (nondimensionalized by $\rho_0 a_0^2$), a friction velocity $v*$ (see White[29]) is defined as,

$$\nu^* = \tau_w^{1/2}, \qquad \left(\overline{\rho} \approx 1\right) \tag{A3}$$

For a parallel flow in a two dimensional channel, the balance between pressure gradient and wall stress leads to,

$$\overline{\beta} = -\frac{d\overline{p}}{dx} = 2\tau_w = 2\left(v^*\right)^2; \qquad \left(\overline{\rho} \approx 1\right) \tag{A4}$$

To find analytical formulas for ν_T and $\overline{u}$, one may start with Eq. (A2). Upon integrating this equation once, it is found,

$$\left(\nu_T + \nu\right)\frac{d\bar{u}}{dy} = -\bar{\beta}y + C \tag{A5}$$

Outside the laminar sublayer, molecular viscosity is unimportant. That is $\nu_T \gg \nu$. Eq. (A5) may be approximated by,

$$\nu_T \frac{d\bar{u}}{dy} = -\bar{\beta}y + C \tag{A6}$$

In the log-layer of the turbulent flow, it is reasonable to assume that $\bar{u}\left(y\right)$ has the form of a log-profile, i.e.

$$u\left(y\right) \simeq \Gamma v^* \log\left(\frac{v^* y}{\nu}\right) + \text{constant} \tag{A7}$$

where Γ is an unknown factor to be determined later. For a standard turbulent boundary layer, $\Gamma = 1/\kappa$ where κ is the Karman constant. But for a fully turbulent channel flow, where turbulence is not restricted to a fluid layer adjacent to the wall, it is more appropriate to leave Γ as a free parameter to be determined later. On substitution of Eq. (A7) imto Eq. (A6), it is found upon integration,

$$\nu_T = \frac{y\left(C - \bar{\beta}y\right)}{\Gamma\nu^*}. \tag{A8}$$

The constant C is found by requiring $\nu_T\left(y\right)$ to be symmetric with respect to the channel walls. That is, $\frac{d\nu_T}{dy} = 0$ at $y = \frac{1}{2}$. This gives $C = \bar{\beta}$. Hence, Eq. (A8) becomes,

$$\nu_T = \frac{\bar{\beta}y\left(1-y\right)}{\Gamma v^*} = \frac{2\nu^*}{\Gamma}y\left(1-y\right) \tag{A9}$$

Now, the mean flow profile may be found by first inserting Eq. (A9) into Eq. (A5). Upon integration and imposing the boundary condition $\bar{u} = 0$ at the walls, it is straightforward to find,

$$\bar{u}\left(y\right) = \frac{\Gamma v^*}{2}\ln\left(\frac{y - y^2 + \frac{1}{4}\alpha}{\frac{1}{4}\alpha}\right); \quad \text{where } \alpha = \frac{4\Gamma v^* \nu}{\bar{\beta}} = \frac{2\Gamma\nu}{v^*} \tag{A10}$$

In this work, the mean velocity profile ahead of the liner is measured in the NASA experiment. It is shown in Fig. A1. It is possible to determine the two unknown parameters of Eq. (A10), namely v^* and Γ, by best fit of the formula to the data. In the literature, there are extensive turbulent channel flow data. White[31] used these data to develop an empirical procedure (Chapter 6 of his book) to find v^* once the mean velocity profile or the averaged mean velocity is known. On applying White's procedure to the NASA data of Fig. A1, it is easy to find that the value of v^* for this set of data is 3.6803 m/s. At this point, the remaining unknown is Γ. Now Γ can be found by choosing its value by best fit of velocity profile of Eq. (A10) to the NASA data. In this way, Γ is found to be equal to 7.75286.

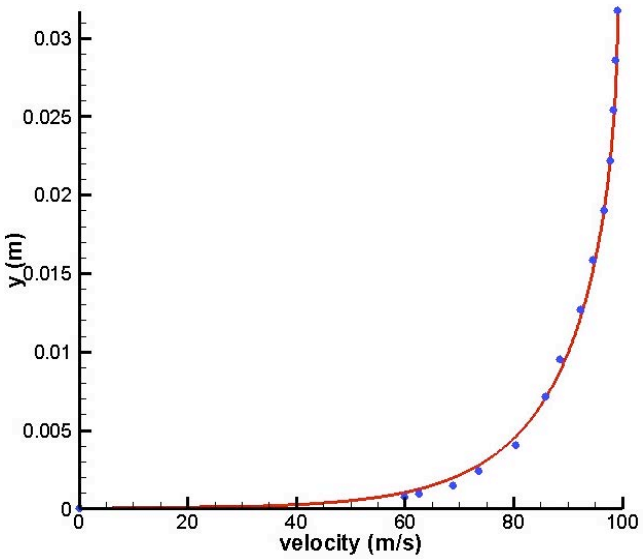

Figure A1. Comparison of semi-empirical velocity profile of Eq. (A10) (full line) and the NASA data (dots).

Fig. A1 shows the comparison of Eq. (A10) (full line) and the NASA measurements (dots) over the bottom half of the channel (total height is 2.5 inches). It is easy to see that the agreement is good. Fig. (A2) shows the corresponding distribution of turbulent eddy viscosity ν_T across the channel according to Eq. (A9).

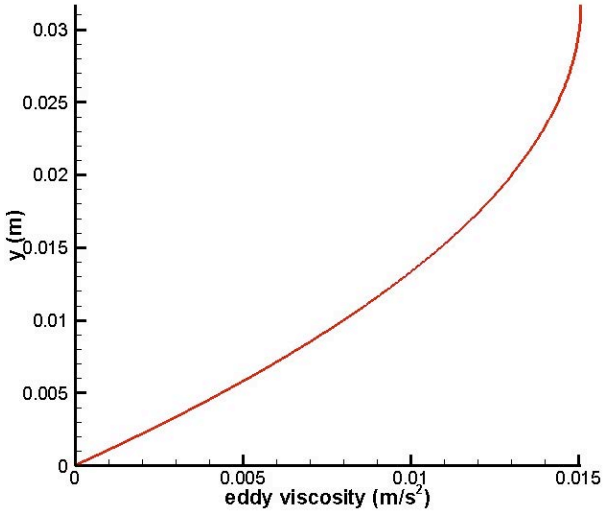

Figure A2. Distribution of turbulent eddy viscosity across the NASA Grazing Flow Impedance Tube according to Eq. (A9).

Acknowledgement

CKWT and NNP wish to acknowledge the support of NASA Langley Research Center through a Phase II SBIR contract.

References

[1]Sivian, L J. , Acoustics impedance of small orifices., *Journal of Sound and Vibration*, Vol. 7, 1935, pp. 94-101.

[2]Ingard, U. and Labate, S., Acoustic circulation effects and the nonlinear impedance orifices, *Journal of the Acoustic Society of America*, Vol. 22, 1950, pp. 211-219.

[3]Ingard, U. and Ising, H. Acoustic nonlinearity of an orifice, *Journal of the Acoustic Society of America*, Vol. 42, 1967, pp. 6-17.

[4]Melling, T. H., The acoustic impedance of perforates at medium and high sound pressure levels, *Journal of Sound and Vibration*, Vol. 29, 1973, pp. 1-65.

[5]Goldman, A. L. and Panton, R. L., Measurement of the acoustic impedance of an orifice under a turbulent boundary layer, *Journal of Sound and Vibration*, Vol. 60, 1976, pp. 1397-1404.

[6]Kompenhans, J. and Ronneberger, D., The acoustic impedance of the orifices in the plate of a flow duct with a laminar or turbulent flow boundary layer, *AIAA paper* 80-0990, 1980.

[7]Kooi, J. W. and Sarin, S.L., An experimental study of the Helmholtz resonator arrays under a turbulent boundary layer, AIAA paper 81-1988, 1981.

[8]Walker, B. E., Charwat, A. F., Correlation of the effects of grazing flow on the impedance of Helmholtz resonators, *Journal of the Acoustical Society of America*, Vol. 72, 1982, pp. 550-555.

[9]Worraker, W. J. and Halliwewll, N. A., Jet engine liner impedance: an experimental investigation of cavity neck flow/acoustics in the presence of a Mach 0.5 tangential shear flow, *Journal of Sound and Vibration*, Vol. 103, 1985, pp. 573-592.

[10]Malmary, C. and Carbonne, S., Acoustic impedance measurement with grazing flow. *AIAA paper* 2001-2193, 2001.

[11]Tam, C. K. W. and Kurbatskii, K. A., Micro-fluid dynamics and acoustics of resonant liners, *AIAA Journal*, Vol. 38, 2000, pp. 1331-1339.

[12]Tam, C. K. W., Kurbatskii, K. A., Ahuja, K. K. and Gaeta, R. J. Jr., A numerical and experimental investigation of the dissipation mechanisms of resonant acoustic liners, *Journal of Sound and Vibration*, Vol. 245, 2001, pp. 545-557.

[13]Zhang, Q. and Bodony, D. J., Numerical simulation of two-dimensional acoustic liners with high speed grazing flow, *AIAA Journal*, Vol. 49, 2011, pp. 365-382.

[14]Tam, C. K. W., Ju, H., Jones, M. G., Watson, W. R. and Parrott, T. L., A computational and experimental study of slit resonators, *Journal of Sound and Vibration*, Vol. 284, 2005, pp. 947-984.

[15]Tam, C. K. W., Ju, H., Jones, M. G., Watson, W. R. and Parrott, T. L., A computational and experimental study of resonators in three dimensions, *Journal of Sound and Vibratiion*, Vol. 329, 2010, pp. 5164-5193.

[16]Zhang, Q. and Bodony, D. J., Numerical investigation and modeling of acoustically-excited flow through a circular orifice backed by a hexagonal cavity, *Journal of Fluid Mechanics*, Vol. 693, 2012, pp. 367-401.

[17]Roche, J. M. Leylekian, L. Delattre, G. and Vuillot, F., Aircraft fan noise absorption: DNS of the acoustic dissipation of resonant liners, *AIAA Paper* 2009-3146, 2009.

[18]Tam, C. K. W., Ju, H. and Walker, B. E., Numerical simulation of a slit resonator in a grazing flow under acoustic excitation, *Journal of Sound and Vibration*, Vol. 313, 2008, pp. 449-471.

[19]Roche, J. M., Vuillot, F. Leyekian, L., Delattre, L. Piot, G. and Simon, F., Numerical and experimental study of resonant liners aeroacoustic absorption under grazing flow, *AIAA paper* 2010-3767, 2010.

[20]Zhang, Q. and Bodony, D. J., Direct numerical simulation of three-dimensional honeycomb liners with turbulent boundary layer, *AIAA paper* 2012-2246.

[21]Bendat, J. S. and Piersol, A. G., *Random Data: Analysis and Measurement Procedures, Wiley-Interscience*, 1971.

[22]Watson, W., Jones, M. and Parrott, T., A Quasi-3-D theory for impedance eduction in uniform grazing flow, *AIAA paper* 2005-2848.

[23]Tam, C. K. W. and Webb, J. C., Dispersion-relation-preserving finite difference scheme for computational acoustics, *Journal of Computational Physics*, Vol. 107, 1993, pp. 262-281.

[24]Tam, C. K. W. and Kurbatskii, K.A., Multi-size-mesh multi-time-step Dispersion-relation-preserving scheme for multiple scales aeroacoustics problems, *International Journal of Computational Fluid Dynamics*, Vol. 17, 2003, pp. 119-132.

[25]Tam, C. K. W. *Computational Aeroacoustics: a wave number approach*. Cambridge University Press, 2012.

[26]Hu, F. Q., A stable, perfectly matched layer for linearized Euler Equations in unsplit physical variables, *Journal of Computational Physics*, Vol. 173, 2001, pp. 455-480.

[27]Tam, C. K. W. and Dong, Z., Wall boundary conditions for high order finite difference schemes in computational aeroacoustics, *Journal of Theoretical and Computationl Fluid Dynamics*, Vol. 6, 1994, pp. 303-322.

[28]Tam, C. K. W. and Dong, Z., Radiation and outflow boundary conditions for direct computation of acoustic and flow disturbances in a nonuniform mean flow, *Journal of Computational Acoustics,* Vol 4, No. 2, 1996, pp. 175-201.

[29]Heller, H. H., Holmes, D. G. and Covert, E. E., Flow-induced pressure oscillations in shallow cavities, *Journal of Sound and Vibration*, Vol. 18, 1971, pp. 545-553.

[30]Kegerise, M. A., Cabell, R. H. and Cattafesta, L. N., Real-time adaptive control of flow-induced cavity tones, *AIAA paper* 2004-0572.

[31]White, F. M. *Viscous Fluid Flow, 2nd edition*, McGraw-Hill, 1991.